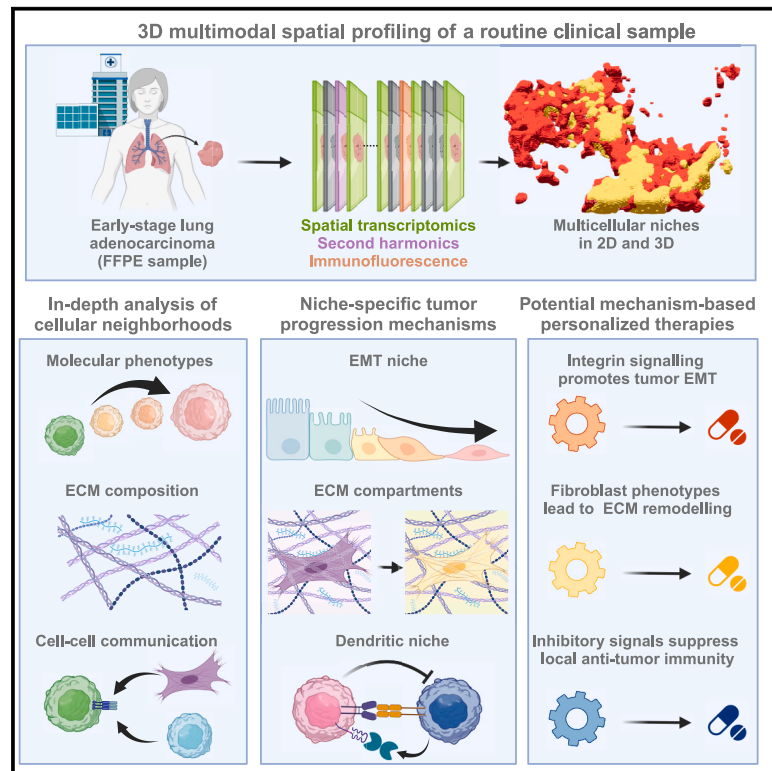


Combining spatial transcriptomics and ECM imaging in 3D for mapping cellular interactions in the tumor microenvironment

Graphical abstract



Authors

Tancredi Massimo Pentimalli,
Simon Schallenberg,
Daniel León-Periñán, ...,
Nikos Karaiskos, Frederick Klauschen,
Nikolaus Rajewsky

Correspondence

rajewsky@mdc-berlin.de

In brief

Pentimalli et al. extend imaging-based spatial transcriptomics to 3D and combine it with ECM profiling. The multimodal analysis of cellular neighborhoods in a clinical lung adenocarcinoma sample revealed potential molecular drivers of tumor progression, ECM remodeling, and immune escape, which could inform microenvironment-directed therapies in the future.

Highlights

- Spatial transcriptomics maps cell types and molecular states to 3D multicellular niches
- 3D receptor-ligand interaction analysis reveals niche-specific communication networks
- ECM imaging links ECM remodeling with gene expression in cellular neighborhoods
- Multimodal analysis reveals druggable mechanisms of tumor progression in a patient sample

Article

Combining spatial transcriptomics and ECM imaging in 3D for mapping cellular interactions in the tumor microenvironment

Tancredi Massimo Pentimalli,^{1,2} Simon Schallenberg,³ Daniel León-Periñán,¹ Ivano Legnini,^{1,4} Ilan Theurillat,¹ Gwendolin Thomas,¹ Anastasiya Boltengagen,¹ Sonja Fritzsche,^{5,18} Jose Nimo,^{2,5,18} Lukas Ruff,⁶ Gabriel Dernbach,^{3,6,7} Philipp Jurmeister,⁸ Sarah Murphy,⁹ Mark T. Gregory,⁹ Yan Liang,⁹ Michelangelo Cordenonsi,¹⁰ Stefano Piccolo,^{10,11} Fabian Coscia,⁵ Andrew Woehler,^{12,13} Nikos Karaiskos,¹ Frederick Klauschen,^{2,7,8} and Nikolaus Rajewsky^{1,2,14,15,16,17,19,*}

¹Laboratory for Systems Biology of Regulatory Elements, Berlin Institute for Medical Systems Biology (BIMSB), Max-Delbrück-Centrum for Molecular Medicine in the Helmholtz Association (MDC), Berlin, Germany

²Charité – Universitätsmedizin Berlin, corporate member of Freie Universität Berlin

³Institute of Pathology, Charité – Universitätsmedizin Berlin, corporate member of Freie Universität Berlin and Humboldt-Universität Berlin, Berlin, Germany

⁴Human Technopole, Milan, Italy

⁵Max-Delbrück-Center for Molecular Medicine in the Helmholtz Association (MDC), Spatial Proteomics Group, Berlin, Germany

⁶Aignostics GmbH, Berlin, Germany

⁷BIFOLD – Berlin Institute for the Foundations of Learning and Data, Berlin, Germany

⁸Institute of Pathology, Ludwig Maximilians Universität, Munich, Germany

⁹NanoString® Technologies, Inc, Seattle, WA, USA

¹⁰Department of Molecular Medicine, University of Padua, Padua, Italy

¹¹IFOM ETS, the AIRC Institute of Molecular Oncology, Milan, Italy

¹²Systems Biology Imaging Platform, Berlin Institute for Medical Systems Biology (BIMSB), Max-Delbrück-Centrum for Molecular Medicine in the Helmholtz Association (MDC), Berlin, Germany

¹³Howard Hughes Medical Institute, Janelia Research Campus, Ashburn, VA, USA

¹⁴German Center for Cardiovascular Research (DZHK), Site Berlin, Berlin, Germany

¹⁵NeuroCure Cluster of Excellence, Berlin, Germany

¹⁶German Cancer Consortium (DKTK), Berlin, Germany

¹⁷National Center for Tumor Diseases (NCT), Site Berlin, Berlin, Germany

¹⁸Humboldt-Universität zu Berlin, Institute of Biology, 10099 Berlin, Germany

¹⁹Lead contact

*Correspondence: rajewsky@mdc-berlin.de

<https://doi.org/10.1016/j.cels.2025.101261>

SUMMARY

Tumors are complex ecosystems composed of malignant and non-malignant cells embedded in a dynamic extracellular matrix (ECM). In the tumor microenvironment, molecular phenotypes are controlled by cell-cell and ECM interactions in 3D cellular neighborhoods (CNs). While their inhibition can impede tumor progression, routine molecular tumor profiling fails to capture cellular interactions. Single-cell spatial transcriptomics (ST) maps receptor-ligand interactions but usually remains limited to 2D tissue sections and lacks ECM read-outs. Here, we integrate 3D ST with ECM imaging in serial sections from one clinical lung carcinoma to systematically quantify molecular states, cell-cell interactions, and ECM remodeling in CN. Our integrative analysis pinpointed known immune escape and tumor invasion mechanisms, revealing several druggable drivers of tumor progression in the patient under study. This proof-of-principle study highlights the potential of in-depth CN profiling in routine clinical samples to inform microenvironment-directed therapies. A record of this paper's transparent peer review process is included in the supplemental information.

INTRODUCTION

In the past decades, the discovery of oncogenic mutations altering tumor-promoting intracellular signaling pathways sparked the development of an ever-growing arsenal of targeted agents that specifically inhibit mutant proteins. Today, in the era

of precision oncology, next-generation sequencing technologies enable the high-throughput screening of druggable mutations, central to selecting the most effective therapeutic approach for individual patients. Nevertheless, tumors are complex ecosystems where tumor cells live in close contact with the surrounding extracellular matrix (ECM), as well as neighboring

malignant and non-malignant stromal and immune cells. Besides oncogenic mutations, cell-ECM and cell-cell interactions affect tumor phenotypes and shape the tumor microenvironment (TME) toward tumor promotion or eradication, thus representing an attractive therapeutic approach.¹ In fact, the ECM provides both the physical substrate for tumor, stromal, and immune cell migration and can affect virtually any hallmark of cancer directly via ECM-receptor interactions and indirectly modulating chemokine and growth factor availability.² At the same time, receptor-ligand interactions between malignant, stromal, and immune cells also affect the balance between tumor growth and suppression, immune recognition and escape, and therapy response and resistance.³ As demonstrated by the efficacy of immunotherapies, blocking specific cell-cell communication axes can rewire the TME and lead to sustained therapeutic responses in selected patients.⁴ Therefore, the in-depth integrative study of ECM composition and cell-cell interactions in the TME is particularly attractive to pinpoint the drivers of tumor progression and identify therapeutic vulnerabilities in individual tumors beyond genetic mutations.

In particular, non-small cell lung cancer (NSCLC), which accounts for >80% of lung cancers, represents a prime example of precision oncology.⁵ Despite the personalized administration of targeted therapies,⁶ therapeutic responses are often short-lived, and NSCLC remains the main cause of cancer-related death.⁷ At the same time, 20% of advanced NSCLC patients respond to immunotherapy, while up to 30% of treated patients suffer from immune-related adverse events.⁸ Therefore, the identification of personalized biomarkers beyond druggable mutations represents an urgent unmet clinical need to maximize therapeutic efficacy and limit toxicity in NSCLC.

Currently, tumor molecular profiling in the clinic relies on the bulk analysis of tumor genomes and transcriptomes, which fails to capture the heterogeneity and spatial organization of the TME. While single-cell omics have been successfully applied to profile the cellular and molecular composition of the TME,⁹ tissue dissociation invariably leads to the loss of position information and fails to profile interactions among neighboring cells. At the same time, the sequential alignment of individual sections stained with hematoxylin and eosin (H&E) staining¹⁰ or profiled with multiplex immunofluorescence¹¹ and imaging mass cytometry¹² enabled the initial exploration of the TME even in 3D at the morphological and cellular level, respectively. However, measuring tens of proteins prevented the simultaneous study of molecular phenotypes and receptor ligand in cellular neighborhoods, central to understanding which cell-cell interactions—among a plethora of well-known ones—drives tumor progression in individual patients. Conversely, spatial transcriptomics (ST) methods map the expression of hundreds to thousands of gene targets in intact tissue sections and have profoundly changed our ability to characterize gene expression in space.¹³ In particular, imaging-based ST methods, such as CosMx Spatial Molecular Imager (CosMx),¹⁴ use *in situ* hybridization probes for the sensitive detection of their targets at single-molecule resolution and enable the high-plex profiling of routinely collected, formalin-fixed paraffin-embedded (FFPE) clinical samples. Nevertheless, high-resolution ST methods have not yet been used for reconstructing FFPE specimens in

3D, and tissue molecular properties have thus far been isolated from the contextual ECM composition.

Here, we present the 3D, multimodal map of a clinical tumor sample measuring the expression of 960 genes with CosMx together with ECM second harmonic generation (SHG) imaging (data can be explored interactively at <http://lung-3d-browser.mdc-berlin.de/>). The computational alignment of consecutive sections using our tool STIM¹⁵ enabled the reconstruction of 3D cellular neighborhoods and captured the organization of the TME in multicellular niches. At the same time, SHG quantified elastin and collagen content in cellular neighborhoods and captured a continuum of ECM remodeling in the TME. Combining SHG with ST then revealed which ECM regulators were expressed by fibroblasts and which fibroblast molecular states were spatially restricted to sites of ECM remodeling. Finally, the combination SHG and 3D ST enabled the in-depth profiling of cellular interactions in the TME and identified which interactions mediated tumor progression *in situ*, including targets of already approved agents. In this proof-of-principle study, we highlight the power of in-depth spatial molecular tumor profiling to pinpoint which among a plethora of well-known mechanisms drives tumor progression in individual patients, central to inform mechanism-based, personalized therapies.

RESULTS

Multimodal study of one aggressive, routinely collected NSCLC tumor in 3D

We focused on an early-stage NSCLC patient, who demonstrated rapid disease progression and aggressive tumor biology (Figure S1A). To reconstruct 3D cellular neighborhoods, we cut 34 consecutive 5 μ m-thick tissue sections from a routinely collected, archival FFPE block (surgical resection specimen from the primary tumor, Figure 1A). We leveraged deep-learning-based classification of tumor, stromal, and normal lung-resident compartments (STAR Methods) of a whole-slide H&E image to select a 16 mm² wide region of interest (ROI) featuring the copresence of both the primary tumor and cancer-associated stroma for ST investigation (Figure 1B). Furthermore, we reasoned that the presence of small-caliber airways crossing the section planes would provide anchoring points for section alignment in 3D. We then collected single-cell resolved ST data from every 6th section (30 μ m section-to-section interval) and profiled intervening sections with complementary modalities, enabling the integrative analysis of tissue morphology, ECM composition, protein markers, and gene expression.

Molecular histology of the TME at single-cell resolution

To gain insights into the spatial organization and crosstalk between tumor, stromal, and immune populations, we performed 1000-plex RNA *in situ* hybridization (ISH) with CosMx and leveraged deep-learning-based cell segmentation of nuclei and plasma membranes to obtain single-cell gene expression profiles (STAR Methods). We profiled 960 cancer-related genes, allowing the simultaneous characterization of cellular identities, transcriptomic states, and cell-to-cell communication in the TME.¹⁴

To assess data quality, we first quantified counts from 20 negative probes (i.e., targeting sequences not present in

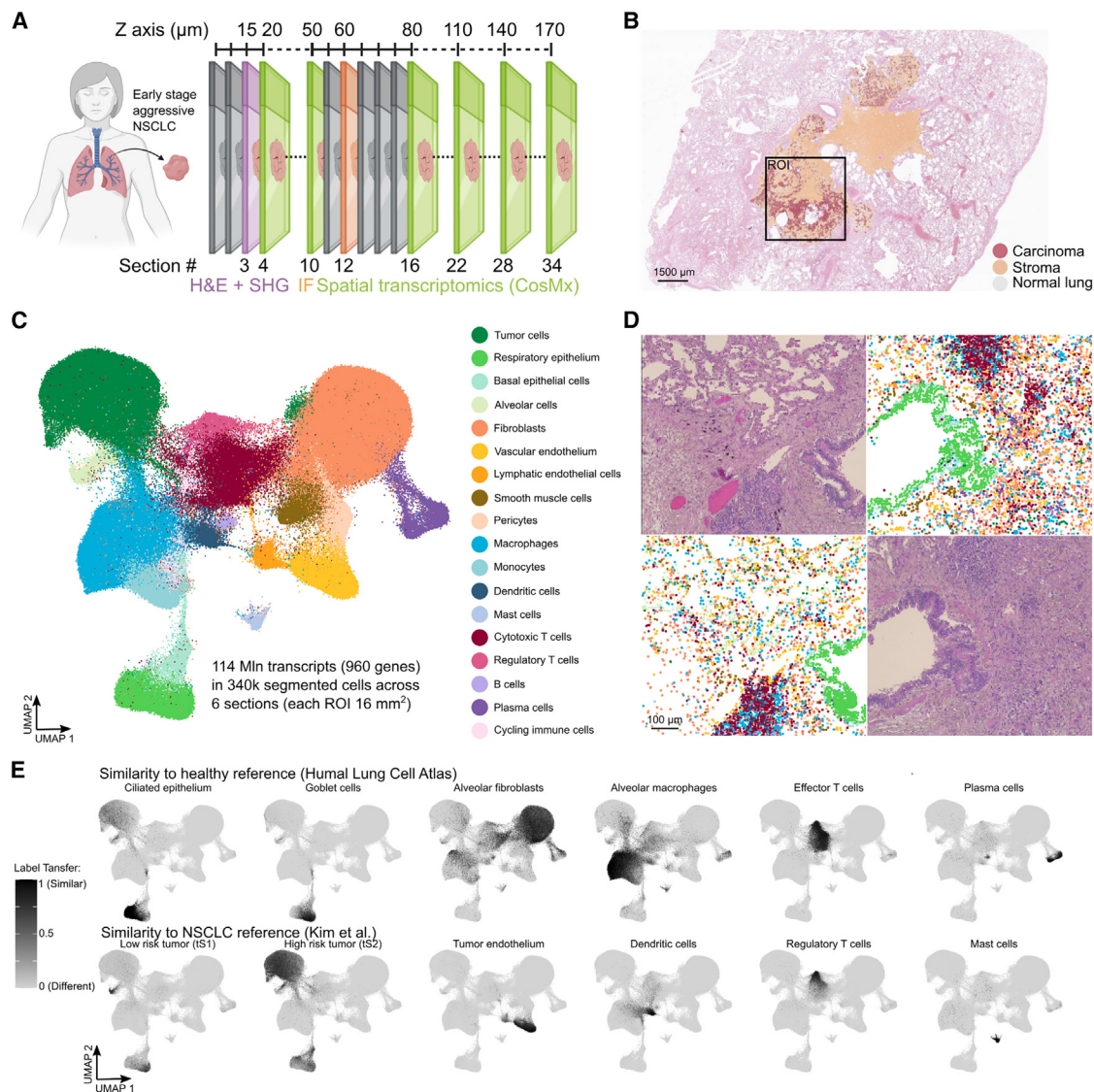


Figure 1. Molecular histology of the TME at single-cell resolution

(A) Experimental design for the 3D reconstruction and multimodal profiling of cellular neighborhoods. 34 consecutive 5 µm sections were cut from one non-small cell lung cancer (NSCLC) tumor block. Second harmonic imaging (SHG, quantifies collagen and elastin), hematoxylin and eosin (H&E, detects tissue morphology), ST (1000-plex RNA *in situ* hybridization with CosMx), and immunofluorescence (IF) were combined for multimodal spatial profiling. Gray: sections collected on a glass slide but not processed.

(B) Deep learning-based identification of a tumor and stroma-rich region of interest (ROI, black square). Semantic segmentation of the whole-slide H&E image in carcinoma (red), stroma (orange), and normal lung (not colored) regions.

(C) 18 epithelial, stromal, and immune cell types compose the TME. UMAP of cellular gene expression colored by cell type identity (CosMx data generated in this study).

(D) Molecular histology matches tissue morphology. Top left and bottom right: H&E staining (section 3). Top right and bottom left: CosMx cells colored by their assigned cell types (section 4).

(E) Congruence of gene expression profiles in segmented cells with single-cell RNA sequencing references. UMAPs of cellular gene expression colored by label transfer scores from healthy¹⁶ and tumor¹⁷ published atlases.

human tissues), which composed only 0.27% of detected molecules, demonstrating highly specific detection of target genes. We then verified the colocalization of pan-cytokeratin (panCK) protein staining and KRT19 transcript ISH signal in the same section (Figure S1B). Overall, we imaged 155,055,865 transcripts distributed in six sequential, non-consecutive ROIs (Figure S1C) and assigned 74.1% of transcripts to 340,644

segmented cells (101 median genes and 198 median transcripts/cell). Near-perfect correlations of total transcript counts confirmed robust gene expression profiling across sections with hierarchical clustering recapitulating section spatial arrangements (Figure S1D).

Unsupervised clustering of gene expression in segmented cells (Figure S1E) identified 18 cell types (Figure 1C), annotated

based on the expression of canonical marker genes (Figure S1F) and IF positivity to panCK staining (Figure S1G). In line with previous reports,¹⁸ tumor cells were characterized by a larger cell size and higher transcript counts. Transferring cell type annotations back to their tissue positions, the spatial patterns of airway epithelial cells (Figure 1D), tumor, stromal, and immune populations corresponded with those evident from routine histology (Figures S1H and S1I). Finally, comparison of gene expression in segmented cells with published single-cell RNA sequencing atlases confirmed the agreement of our cell type annotations with healthy lung^{16,19} and NSCLC atlases¹⁷ (Figure 1E).

In summary, we generated a high-quality, single-cell-resolved molecular atlas of the TME, encompassing more than 340,000 cells from 18 epithelial, stromal, and immune cell types, and proceeded to explore their 3D neighborhoods.

3D neighborhoods enable the unbiased identification of TMEs multicellular niches

To reconstruct 3D cellular neighborhoods, we leveraged STIM,¹⁵ which employs state-of-the-art computer vision techniques, to computationally align ST data and generate a 3D molecular map of the TME at single-cell resolution. Owing to the precise positioning of the ROIs during data collection, relatively minor transformations were required for 3D image registration (median cell displacement: $\sim 42\ \mu\text{m}$) (Figure S2A), which would, however, alter 3D cellular neighborhoods if uncorrected. Furthermore, visualization of respiratory epithelium cells in 3D revealed the expected airway lumen continuity (Figure 2A).

As cellular activities and molecular profiles are shaped by the surrounding tissue microenvironment,¹³ we defined 3D neighborhoods for each cell as a spherical space encompassing all cells located within a $50\ \mu\text{m}$ center-to-center distance (Figure 2B) and grouped cells sharing the same tissue microenvironment—regardless of their gene expression. Unbiased clustering of 3D neighborhoods revealed 10 multicellular niches sharing a specific neighborhood composition (Figures 2C, S2B, and S2C). These included both lung-resident epithelial (i.e., “airways” and “alveoli”) and stromal (i.e., “smooth muscle”) niches and TME-specific tumor, stromal, and immune niches (Figure 2D). 3D neighborhoods distinguished the “vascular stroma”—rich in vascular endothelium and pericytes—from the “desmoplastic stroma,” featuring the highest fibroblast and plasma cell density. High numbers of tumor cells characterized the 3D neighborhoods of two distinct niches, which we annotated as “tumor core” and “tumor surface.” Therefore, the tumor bed was composed of the tumor core, featuring a higher cellular density but a lower cellular diversity (Figure S2D) (i.e., dominated by tumor cells), and the tumor surface with higher fibroblasts, macrophages, and cytotoxic T cell (CTL) counts, compatible with its position at the tumor-stromal boundary. Tumor cells were also abundant in “dendritic cell niches” and “macrophage niches” but not in “T cell niches.”

Mapping niche annotations back to their tissue positions allowed the comparison with manual annotations of routine H&E histology by an experienced pathologist. Multicellular niches closely followed tissue architectures visible by routine histology, including airways, alveoli, lymphocyte aggregates, tissue fibrosis, and smooth muscle in the tunicae of larger blood vessels (Figure 2E). Furthermore, multicellular niches distinguished

smaller vessels from the surrounding stroma and provided a more granular annotation of tumor, immune, and stromal niches.

In summary, we leveraged our 3D tumor atlas to analyze over 200,000 cellular neighborhoods and identify 10 distinct, repeating, and spatially organized multicellular niches in the TME. Niches corresponded to and extended expert annotations of morphological tissue structures, highlighting the ability of 3D neighborhoods to capture the spatial organization of the TME.

3D neighborhoods improve the identification and spatial mapping of intratumoral immune niches

As cells live and interact in 3D tissues, we hypothesized that analyzing 3D cellular neighborhoods would improve our ability to study multicellular niches. Therefore, we systematically compared 2D and 3D neighborhoods in the patient under study (Figure 3A). By design, 3D neighborhoods included cells from the sections immediately above and below the z plane (STAR Methods), comprising a 2.28-fold larger area than their 2D counterparts. As expected, 2D neighborhoods featured a lower number of neighbors and lower cell type diversity than their 3D counterparts (median of 71 cells from 9 cell types/neighborhood in 3D vs. 32 cells from 7 cell types in 2D, $p < 0.005$), confirmed by a lower alpha diversity—a common measure of species richness in ecology studies (median Chao index 3D: 10.5 vs. 2D: 8, $p < 0.005$) (Figure 3B).

Comparing the ability of 2D neighborhoods to capture the TME spatial organization with their 3D counterparts, we noted that 2D niches largely corresponded to 3D ones and included a “macrophage-rich stroma” (Figures 3C and S3A–S3C). However, 2D niches failed to identify “dendritic cell niches,” which were validated by IF staining (Figure S3D). In fact, cells assigned to dendritic cell niches in 3D were mainly reassigned to the tumor surface (51.2%) and T cell niches (23.6%) in 2D. Extending such a comparison to all multicellular niches, we observed that 64.1% of cells were assigned to the same niche in 2D and 3D overall. However, rates varied across niches, and T cell niches featured the lowest concordance (46.2%). In 2D, 35.3% of cells assigned to T cell niches in 3D were reassigned to the desmoplastic stroma with a consequent reduction in niche size (32,272 cells in 3D vs. 17,355 cells in 2D) (Figure 3D). Leveraging 3D rendering (STAR Methods), we compared the spatial localization of T cell niches in 2D and 3D and observed that 3D-specific cells surrounded and formed bridges between seemingly disconnected patches of T cell niches already identified in 2D, restoring their spatial continuity (Figure 3E).

Finally, we sought to further investigate the 3D spatial relationships between the tumor surface and immune niches in TME. We confirmed how the “tumor surface” precisely interlocked and covered the “tumor core” in 3D and demonstrated the spatial continuity of the tumor surface with dendritic and macrophage niches (Figure 3F). By contrast, T cell niches were not embedded in the tumor surface but rather located further away in proximity to larger airways or dispersed in the stroma.

Overall, the study of 3D cellular neighborhoods revealed the complexity and richness of cellular microenvironments. In the patient under study, 3D analyses improved the spatial mapping

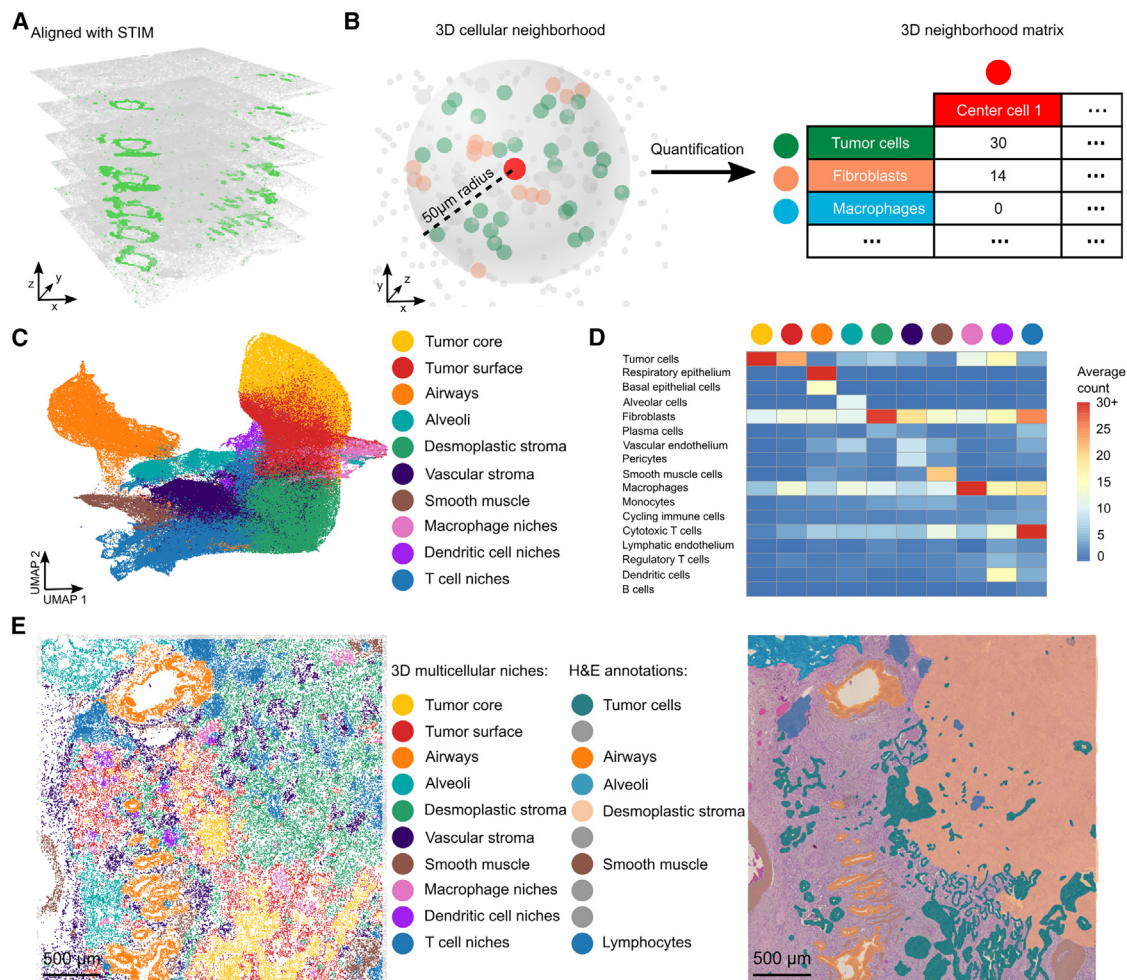


Figure 2. 3D neighborhoods identify multicellular niches in the TME

(A) Airways cross multiple sections in 3D. 3D plot of the 6 CosMx sections after registration with STIM. Green: respiratory epithelium cells, gray: other cell types. Axes are scaled to the same length for visualization purposes.

(B) Design and analysis of 3D cellular neighborhoods. Left: exemplary 3D neighborhood. Red: center cell, dark green: tumor cells, orange: fibroblasts, gray: other cell types. Right: quantification of cell types in 3D neighborhoods is used to build the 3D neighborhood matrix. Tumor cells, fibroblasts, and macrophages are shown out of 18 cell types quantified.

(C) The TME is formed by lung-resident, tumor, stromal, and immune multicellular niches. UMAP of 3D cellular neighborhoods and colored by 3D niche assignments. Cells are grouped based on their 3D neighborhood composition, regardless of their gene expression.

(D) The composition of 3D neighborhoods guides multicellular niche annotation. Heatmap of niche-specific average cell type counts in 3D neighborhoods. Color scale is clipped to 30 for visualization purposes.

(E) 3D multicellular niches capture the spatial organization of the TME. Comparison of 3D niche spatial localization (left, section 10) with pathologist manual annotations of H&E tissue domains (right, section 3).

of T cell niches and distinguished dendritic cell niches from the surrounding tumor surface.

3D neighborhoods enable the systematic study of ligand-receptor interactions in TMEs multicellular niches

The TME is a dynamic tissue shaped by the crosstalk between tumor, stromal, and immune cells.³ To systematically study cell-cell communication between proximal cells, we leveraged the sensitive detection (1–2 molecules/cell¹⁴) of receptor and ligand transcripts in 3D cellular neighborhoods and estimated the spatial activity of 480 receptor-ligand pairs annotated in

the CellChat database²⁰ (Figure 4A). To identify ligands that could drive the spatial organization and function of specific multicellular niches, we further grouped receptor-ligand pairs into 165 ligand-based axes and quantified the signal received by each individual cell from its 3D neighbors (max 50 µm center-to-center distance, Methods). Comparing ligand activities within and outside each niche, we identified 96 ligands to be enriched ($\log_2FC > 0.5$) in at least one niche (Figure 4A). These included well-known endothelial (ESAM and CDH5) and pericyte (PECAM1) cell-cell adhesion molecules in both vascular and alveolar niches (Figure 4B), as well as PDGFB interactions, restricted to vascular niches (Figure 4C). At the same time,

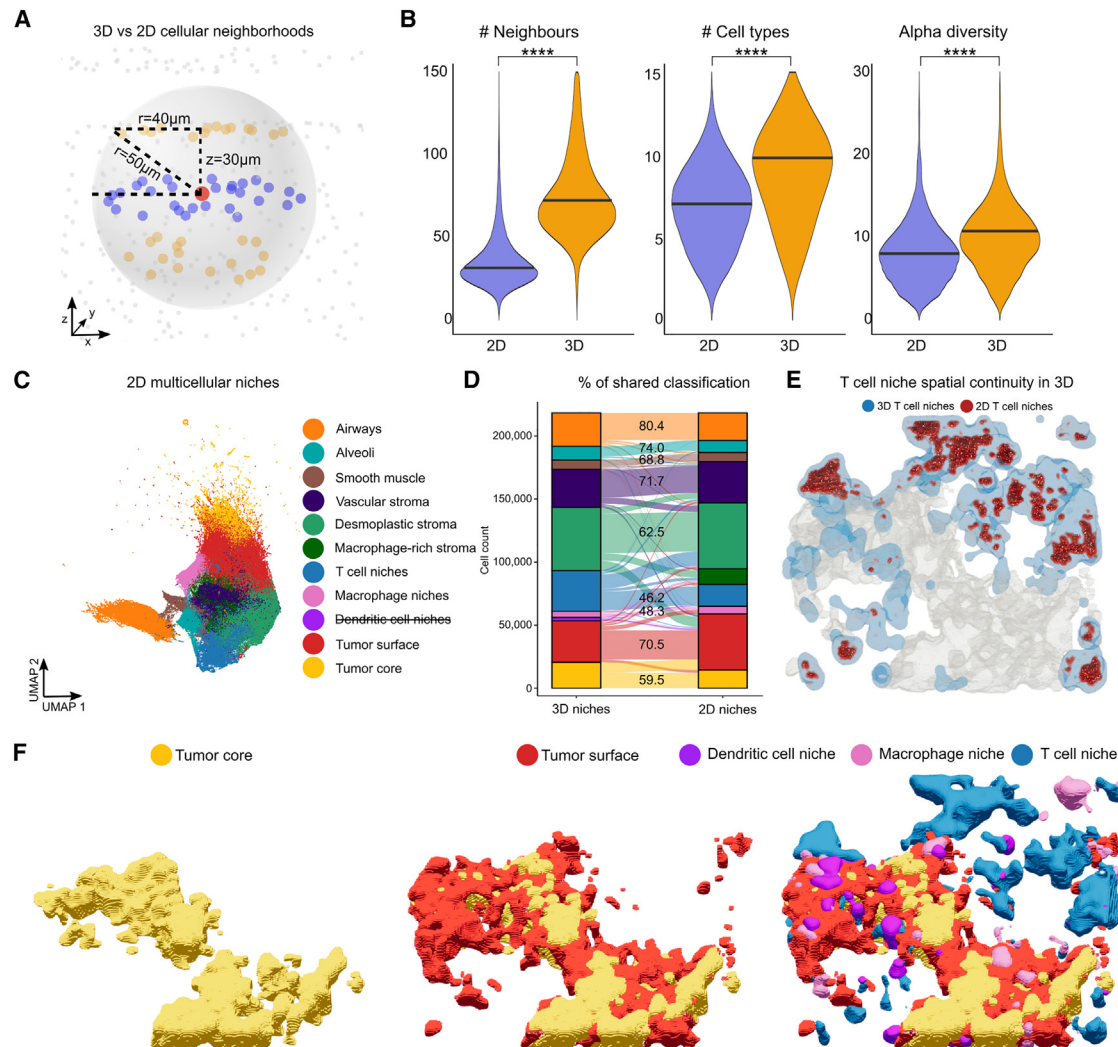


Figure 3. 3D neighborhoods improve the identification and spatial mapping of immune niches

(A) Design of 2D and 3D cellular neighborhoods. Cells in a 50 μm -radius circle around the center cell compose its 2D neighborhood (blue), while cells in a 40 μm -radius circle in the sections above and below the center cell are unique to its 3D neighborhood (orange).

(B) 3D neighborhoods are richer than their 2D counterparts. Distributions of the total number of neighbors (left), unique cell types (middle), and alpha diversity (right) for each cellular neighborhood in 2D (blue) and 3D (orange). ****: t test p values < 0.005 , $n = 218,378$.

(C) Dendritic cell niches are only identified in 3D. UMAP of 2D cellular neighborhoods colored by 2D multicellular niche assignments.

(D) T cell niches have the lowest 2D-3D concordance. Alluvial plot of multicellular niche assignments. Lines follow the same cell in 3D (left) and 2D (right). Color legend in (C).

(E) 3D neighborhoods capture the spatial continuity of T cell niches. Blue: 3D surface rendering of "T cell niches," red: cells assigned to "T cell niches" in 2D, gray: "tumor core and surface."

(F) 3D neighborhoods reveal the 3D spatial relationships between multicellular niches in the TME. 3D rendering reveals how the "tumor surface" (red) covers the "tumor core" (yellow). "Dendritic cell niches" (purple) and "macrophage niches" (pink) are embedded in the tumor surface, while "T cell niches" (blue) are found mainly outside of the tumor bed.

epithelial adhesion molecules (CDH1) and tumor-promoting EFNA1 and AREG signaling were restricted to tumor bed (Figure 4D), while pro-fibrotic ligands (IGF1 and FGF7) and collagen-receptor interactions were enriched in the desmoplastic stroma. In line with their role in the recruitment (i.e., chemotaxis) of specific immune cell populations, the T cell chemoattractant CCL5 (also known as RANTES)²¹ was enriched in T cell niches, while CCL3 (also known as macrophage inflammatory protein 1-alpha) was restricted to macrophage niches. On

the other hand, CCL19, which regulates the homing and retention of CCR7+ dendritic and T cells in lymphoid tissues,²² marked the location of both dendritic and T cell niches in the TME (Figure 4E).

Overall, 3D neighborhoods enabled the systematic study of receptor-ligand interactions between physically proximal cells and revealed which ligand activities were spatially organized within multicellular niches, including well-known drivers of niche-specific cellular composition and functions.

TME.²⁴ To investigate immunomodulatory signals in the patient under study, we focused on the 15 receptor-ligand pairs spatially localized to dendritic cell niches (Figure S4C). In addition to chemokine-receptor pairs (e.g., CCL19-CCR7 and CXCL9-CXCR3), we identified the specific enrichment of key immune checkpoints.

We then leveraged the directionality of signaling in 3D neighborhoods to map the cellular communication networks underlying such interactions (Figure 4F). For example, fibroblasts emerged as the main senders of CCL19-CCR7 interactions and lymphatic endothelial cells of CCL21, suggesting their central role in the formation and/or maintenance of this niche. At the same time, tumor cells were the only cell type that did not act as a receiver of chemokine signals, compatible with their role in the induction of—rather than their recruitment to—dendritic cell niches. Tumor cells instead acted as the main senders of macrophage inhibitory factor (MIF), a potent chemoattractant known to promote the recruitment and immunosuppressive reprogramming of APCs in in NSCLC.²⁵ Supporting its central role in shaping anti-tumoral immunity, MIF inhibition decreased Tregs and promoted CTL infiltration in a melanoma lung metastasis model.²⁶

In turn, DCs—and macrophages to a lesser extent—were engaged in immunosuppressive interactions, both directly inhibiting CTL activity through the CD274-PDCD1 (PD-L1/PD-1) and LGALS9-HAVCR2 (Galectin-9/Tim-3) axes and indirectly by promoting Tregs activity through CD80-CTLA4 interactions. At the same time, CTL accumulated in T cell ($\log_2FC = 1.52$) and dendritic cell niches ($\log_2FC = 0.43$) but failed to infiltrate the tumor core ($\log_2FC = -2.74$) (Figure S4D). Such compartmentalized immune infiltrate is often the result of highly effective immunosuppressive mechanisms able to prevent immune-mediated tumor eradication²⁷ but is predictive of immune checkpoint inhibitor efficacy, given the high numbers of infiltrating T cells ready to attack tumor cells once the immunosuppressive signaling axes have been silenced.^{24,28}

Taken together, 3D neighborhoods mapped receptor-ligand interaction networks in dendritic cell niches, where anti-tumoral immune responses are orchestrated (Figure 4G). As several agents targeting these interactions are already approved for the treatment of NSCLC (e.g., nivolumab and ipilimumab),⁶ our analysis may provide the molecular rationale for their therapeutic targeting in the patient under study.

Second harmonic imaging enables the study of the ECM in cellular neighborhoods

Cellular behaviors are controlled by mechanical and molecular interactions with both their cellular neighbors and the surrounding ECM²⁹; therefore, we integrated our 3D molecular atlas with measurements of ECM composition in cellular neighborhoods. In the lung, elastin and collagen are the major ECM components.³⁰ Thanks to their optical properties, elastin and collagen fibers can be quantified with high specificity using second harmonic imaging (SHG),³¹ a popular label-free method for the spatial analysis of ECM composition. Aligning SHG with single-cell-resolved ST data in two consecutive sections, we systematically investigated the relationship between ECM composition and molecular phenotypes within cellular neighborhoods (STAR Methods).

The TME was characterized by a heterogeneous ECM that closely followed the spatial distribution of main tissue structures, including airways, blood vessels, alveoli, and the desmoplastic stroma (Figure 5A), which was validated using Verhoeff's Van Gieson staining of collagen and elastin fibers (Figure S5A). In terms of ECM composition, cellular neighborhoods are distributed along a continuum, from elastin rich/collagen poor to an elastin poor/collagen rich (Figure 5B). To group cells living in a similar ECM, we unbiasedly clustered cells based on the composition of their surrounding ECM. We identified 3 ECM compartments using k-means clustering (Figure S5B): one elastin-rich “homeostatic,” one elastin and collagen poor “degraded,” and one collagen rich “desmoplastic” ECM compartment. As a positive control, mapping ECM compartments back to their tissue positions revealed a clear spatial separation (Figure 5C), which closely resembled the original SHG images and followed the spatial distribution of multicellular niches and pathologist annotations (Figure 2E). Comparing the observed and expected cell-type frequencies (based on a random distribution, see STAR Methods), we quantified cell type enrichments in specific ECM compartments (Figure S5C). Lung-resident epithelial (alveolar cells $\log_2FC = 1.23$, basal epithelial cells $\log_2FC = 1.07$, and respiratory epithelium $\log_2FC = 1.02$) and vascular populations (smooth muscle $\log_2FC = 0.76$, pericytes $\log_2FC = 0.53$, and vascular endothelium $\log_2FC = 0.60$) were strongly enriched in the homeostatic ECM, while tumor cells ($\log_2FC = 1.20$) were enriched in the degraded ECM and plasma cells ($\log_2FC = 0.82$) in the desmoplastic ECM, in line with their abundance in the desmoplastic stroma niche and their emerging role as promoters of lung fibrosis.³²

Overall, this highlights the ability of SHG to capture ECM dynamics in TME cellular neighborhoods, where ongoing remodeling during tumor progression results in the degradation of the elastic lung ECM and its progressive replacement by a stiff, collagen-rich matrix.³³

Multimodal spatial profiling links fibroblast phenotypes and ECM compartments

Fibroblasts are the major ECM producers and organizers throughout the body.³⁴ In the TME, cancer-associated fibroblasts (CAFs) are responsible for the increased matrix stiffness and architectural remodeling typical of the malignant ECM.³⁵ CAFs, however, display a remarkable heterogeneity,³⁶ also playing critical roles in the shaping of local immune responses mediating the recruitment and activation of immune populations in the TME.³⁷

In the patient under study, fibroblasts were the most abundant cell type and—despite being enriched in the desmoplastic ECM ($\log_2FC=0.38$, 44.5% of fibroblasts)—were highly represented in the degraded (32.8%) and homeostatic compartments (22.7%) as well. Therefore, we hypothesized that the observed changes in ECM composition could be mediated by fibroblast functional heterogeneity, rather than by their abundance. The unbiased analysis of fibroblast molecular profiles ($n = 62,604$) identified six transcriptomic states (Figure 5D), which we annotated through literature-informed review of their marker genes (STAR Methods, Figure S5D). Their spatial distribution was non-homogeneous across the TME (Figure 5E) but showed preferential enrichments in both ECM compartments and multicellular niches

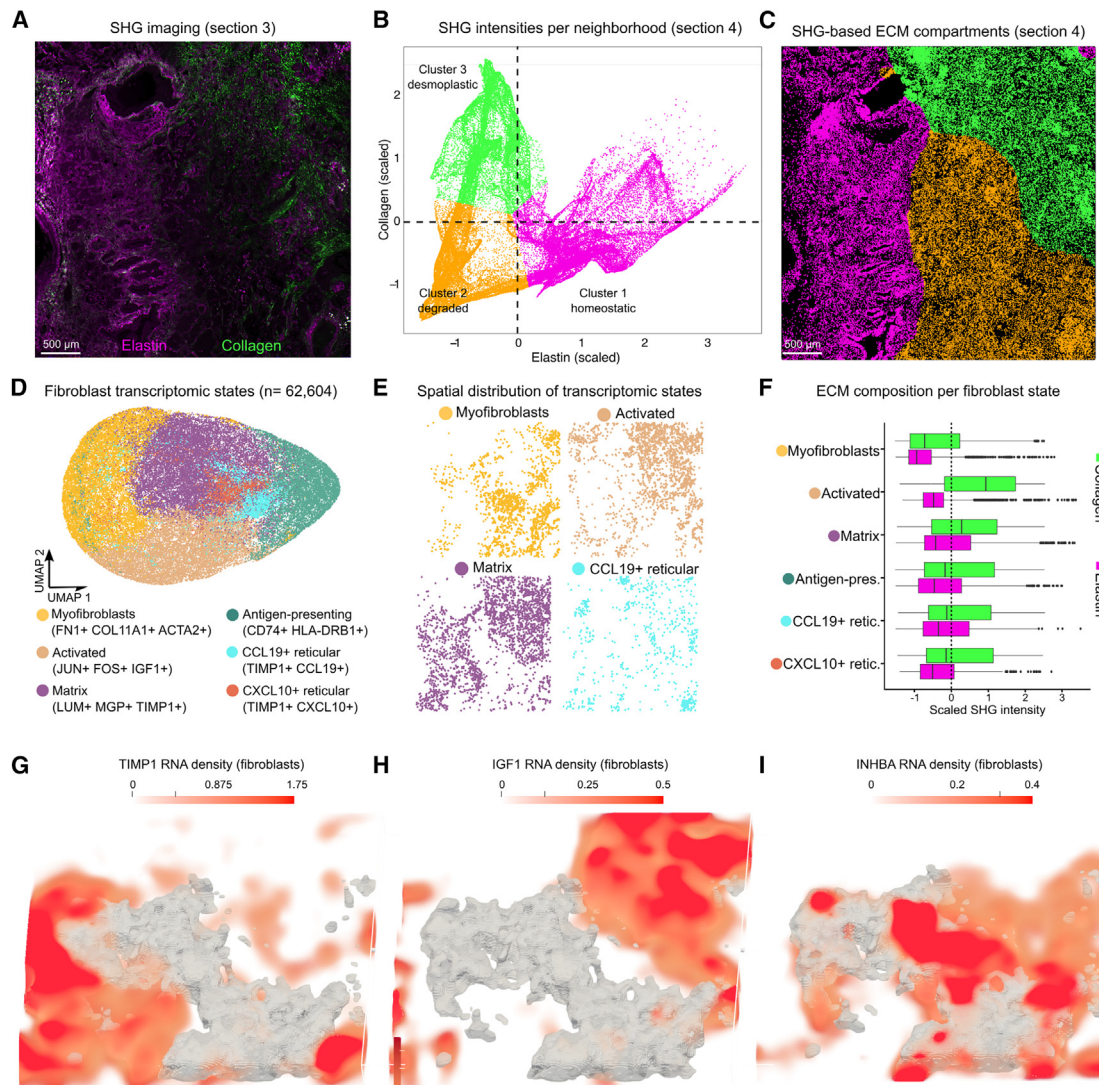


Figure 5. Second harmonic imaging links ECM compartments with fibroblast phenotypes *in situ*

(A) Second harmonic generation (SHG) imaging captures extracellular matrix (ECM) remodeling in the TME. Collagen (green) and elastin (magenta) fibers were quantified by SHG in section 3.
(B) SHG enables the unbiased assignment of cells to specific ECM compartments. Quantification of elastin (x axis) and collagen (y axis) fibers in cellular neighborhoods (50 x 50 μm area around each cell centroid) highlights the transition from an elastin-rich, collagen-poor homeostatic ECM to a collagen-rich, elastin-poor desmoplastic ECM. Cells are colored by k-means cluster assignment ($k = 3$).
(C) SHG spatially maps ECM compartments in the TME. Cells in section 4 are colored by their ECM cluster assignments. Color legend in (C).
(D) Fibroblasts feature heterogeneous transcriptomic phenotypes in the TME. UMAP of fibroblast gene expression colored by transcriptomic clusters.
(E) Fibroblast phenotypes are spatially organized in the TME. Spatial distribution of fibroblast transcriptomic clusters (section 4).
(F) Fibroblast phenotypes are linked with ECM remodeling. Boxplot of collagen and elastin fiber abundance in fibroblast neighborhoods across fibroblast clusters.
(G–I) Fibroblast expression of ECM regulators is spatially organized within ECM compartments. 3D volumetric rendering of TIMP1 (G), IGF1 (H), and INHBA (I) fibroblast expression density.

(Figures S5E and S5F). Quantification of the collagen and elastin signals in fibroblast neighborhoods highlighted a close correspondence between fibroblast phenotypes and ECM composition (Figure 5F): *FN1+ COL11A1+ ACTA2+* “myofibroblasts” were spatially restricted to the degraded ECM in the tumor bed and surrounded by the lowest collagen signal, while *JUN+ FOS+ IGF1+* activated fibroblasts in the desmoplastic ECM surrounded by the highest collagen levels. On the other hand, *LUM+ MGP+ TIMP1+* “matrix fibroblasts,” *CD74+ HLA-DRB1+* “anti-

gen-presenting,” *TIMP1+ CCL19+* and *TIMP1+ CXCL10+* “reticular” fibroblasts were surrounded by a homeostatic ECM. At the same time, antigen-presenting fibroblasts preferentially homed to macrophage niches, while reticular fibroblasts to dendritic and T cell niches, compatible with their role in shaping immune responses in the TME, rather than ECM metabolism.

Seeking to pinpoint which fibroblast factors were involved in the active metabolism of the surrounding ECM, we focused on “matrisome” genes: the ensemble of structural ECM

components (i.e., collagens, proteoglycans, and glycoproteins), ECM regulators (i.e., matrix metalloproteases), and ECM-affiliated proteins (i.e., ECM-bound secreted factors).³⁸ 23 out of 241 measured matrisome genes were enriched in a specific ECM compartment (Figure S5G). Basal lamina collagens *COL4A1*, *COL4A2*, *COL15A1*, and *COL18A1*³⁰ in the homeostatic ECM, fibril-associated *COL14A1*³⁹ were enriched in the desmoplastic ECM, while FN1—a key ECM constituent during embryonic development, wound healing, and tumorigenesis⁴⁰—and *COL11A1*—typically detected at the tumor invasive front⁴¹—in the degraded ECM. In addition to ECM constituents, the integrative analysis of ECM composition and fibroblast gene expression revealed which ECM regulators were restricted to specific ECM compartments, such as *TIMP1* (Figure 5G), a broad-spectrum inhibitor of MMPs,⁴² in the homeostatic ECM, the pro-fibrotic ligands *IGF1* (Figure 5H) and *CXCL12* in the desmoplastic ECM, and the ECM-associated signaling molecules *INHBA* (Figure 5I), *IGFBP5*, and *VEGFA* in the degraded ECM. Notably, the simultaneous upregulation of *FN1*, *COL11A1*, *INHBA* (Inhibin A, a member of the TGF β superfamily), and *VEGFA* was recently identified in a CAF subset restricted to hypoxic TME regions of colorectal cancer patients and linked with poor patient prognosis.⁴³

Overall, the multimodal profiling of fibroblast neighborhoods revealed the close association of their transcriptomic states with specific ECM compartments and multicellular niches and enabled the identification of key local ECM constituent and regulators. Given the multiple pro-invasive ECM factors detected in the tumor bed, we further investigated the relationship between ECM composition, fibroblast, and tumor phenotypes in the TME.

Multimodal analysis of tumor infiltration reveals an EMT niche at the tumor surface

The ability of cancer cells to detach from the epithelial sheet and infiltrate the adjacent stroma (i.e., “invasiveness”) is a hallmark of malignant tumors and essential for metastatic dissemination.⁴⁴ Quantifying the 3D niche assignments of 38,804 tumor cells, we noted that, while most tumor cells were comprised within the tumor bed, more than 9,000 tumor cells (24.0%) infiltrated other multicellular niches (Figure S6A) and were especially abundant in the desmoplastic stroma (Figure 6A).

To unbiasedly reconstruct the phenotypic transitions of tumor cells in the TME, we leveraged pseudotime, a popular approach in the single-cell transcriptomics field to reconstruct dynamic molecular processes. We first ranked tumor cells from 0/early to 1/late pseudotime based on gene expression similarity and identified which genes were underlying these tumor phenotypes. Compatible with epithelial-to-mesenchymal transition (EMT),⁴⁵ epithelial cell adhesion molecules *CDH1* and *EPCAM* were expressed in early pseudotime cells and then downregulated in tumor cells later in pseudotime (Figure 6B), while *ITGB6*⁴⁶ and *COL3A1*⁴⁷ and other mesenchymal markers were upregulated in late pseudotime tumor cells (Figure 6B).⁴⁵

Combining pseudotime and 3D niche assignments, we investigated the spatial distribution of EMT in tumor cells across the TME and noted how EMT was progressively activated when transitioning from the tumor core to the tumor surface and stroma-infiltrating tumor cells (median pseudotime scores:

0.39, 0.50, and 0.85, $p < 0.05$) (Figure 6C). Therefore, “pseudospace” (intended as distance from the tumor bed) closely followed pseudotime, as cells in the tumor bed (i.e., with early pseudospace) featured an epithelial phenotype (i.e., early pseudotime), and stroma-infiltrating tumor cells (i.e., extending beyond the tumor bed) featured both a late pseudospace and pseudotime. However, numerous cells in the tumor bed already showed a mesenchymal phenotype (i.e., late pseudotime) despite their localization in the tumor bed (i.e., early pseudospace). Notably, these mesenchymal tumor cells did not distribute uniformly across the tumor core and surface but rather concentrated in one specific region at the interface with the desmoplastic stroma (Figure 6D). There, the 3D density of pseudotime scores peaked (Figures S6C and S6D), and IF validated the presence of panCK+ CDH1^{low} cells (Figure S6E). The observed discrepancy between early pseudospace and late pseudotime suggests that tumor cells acquire pro-invasive molecular phenotypes in the EMT niche before invading the surrounding stroma.

Mechanotransduction pathways mediate cellular responses to mechanical stimuli and are central to tumor progression, from the initial malignant transformation⁴⁸ to tissue invasion and metastasis.⁴⁹ ECM stiffening, which typically accompanies solid tumors, is indeed a powerful inducer of both tumor EMT⁴⁶ and migration (i.e., “durotaxis”).⁵⁰ Therefore, we investigated the relationship between EMT status and ECM composition in tumor neighborhoods (Figure 6E). While tumor cells infiltrating the stiff, desmoplastic stroma did feature a mesenchymal phenotype, tumor cells in the EMT niche lived in a collagen-poor ECM similar to the rest of the tumor bed (Figure 6F). Therefore, while collagen deposition, which is the main determinant of tissue tension, may sustain EMT in infiltrating tumor cells, it cannot explain EMT induction in the EMT niche. We thus searched for additional factors that were spatially restricted to the EMT niche to understand which mechanisms could trigger tumor invasion.

A wound healing-like communication network activates tumor integrins in the EMT niche

Tumor invasion represents the first step in the metastatic cascade—the major cause of cancer-related death—therefore, mechanistic understanding of the initial steps of tumor invasion is central to the accurate prediction and early interception of tumor dissemination.⁵¹ We investigated whether tumor cells in the EMT niche upregulated specific genes that could serve as early tumor invasion biomarkers. Comparing gene expression in tumor cells inside and outside the EMT niche (Figure S7A), we identified *NDRG1* and *LGALS1* as the genes with the strongest differential expression (Figure 7A). N-myc downstream-regulated gene 1 (NDRG1) promotes stem-like properties in NSCLC cells⁵² and recently emerged as the most specific marker of early brain metastasis (<10 months after diagnosis) in NSCLC patients.⁵³ In the patient under study, who presented with brain metastasis 11 months after diagnosis, we show that *NDRG1* expression is not only enriched but almost spatially restricted to tumor cells in the “EMT niche” (Figure 7B), supporting their involvement in tumor dissemination. *LGALS1* (Galectin-1) was also spatially restricted to the “EMT niche” (Figure 7C). While *NDRG1* is a modulator of intracellular signaling pathways,

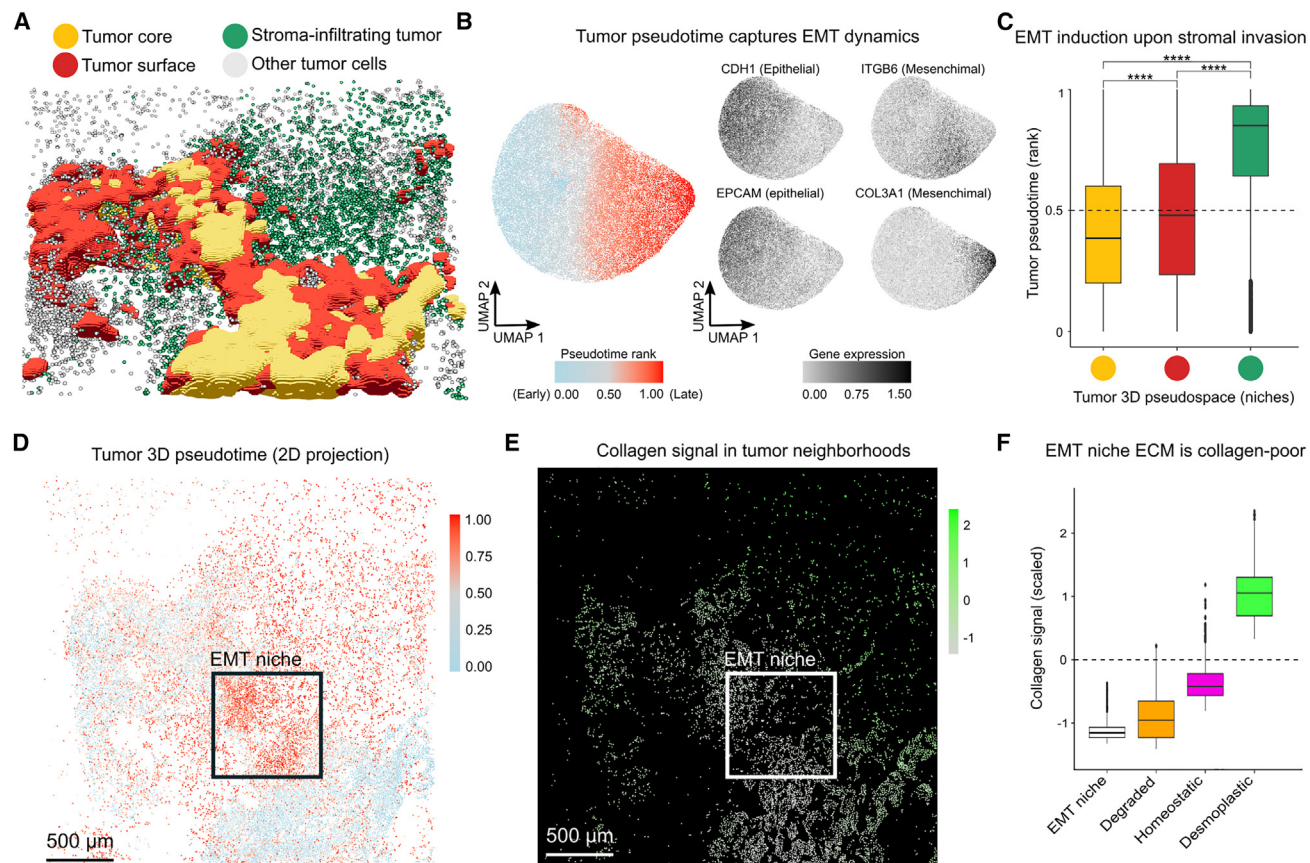


Figure 6. Multimodal analysis of tumor neighborhoods identifies an EMT niche at the tumor surface

(A) 3D neighborhoods reveal numerous stroma-infiltrating tumor cells. 3D rendering of the tumor bed highlights tumor cells extending beyond the tumor surface into the surrounding stroma.

(B) Pseudotime captures tumor epithelial-to-mesenchymal (EMT) dynamics. UMAPs of tumor cell transcriptomic profiles colored by pseudotime rank (left) and the SCT-normalized expression of pseudotime-associated EMT marker genes.

(C) EMT is activated progressively from the tumor core to the desmoplastic stroma. Boxplot of the pseudotime rank of tumor cells in the tumor core, surface, and desmoplastic stroma. ****: t test p values < 0.005 , $n = 38,804$.

(D) Tumor EMT is upregulated not only in the desmoplastic stroma but already in one region of the tumor surface. Spatial distribution of pseudotime rank scores reveals numerous mesenchymal tumor cells in the EMT niche (black box).

(E) Infiltrating tumor cells are surrounded by a stiff ECM. Spatial plot of collagen fiber abundance in tumor cell neighborhoods.

(F) Matrix stiffness accompanies tumor EMT in the desmoplastic stroma but cannot explain its induction in the EMT niche. Boxplot of collagen fiber abundance in tumor cell neighborhoods across the EMT niche and ECM compartments.

LGALS1 acts extracellularly and functions as a switch between the inflammatory and tissue repair phases of wound healing.⁵⁴

LGALS1 promotes both myofibroblast migration and activity⁵⁵ and M1-to-M2 macrophage conversion while inhibiting T cell recruitment.⁵⁴ Accordingly, the cell type composition of the EMT niche differed from the rest of TME, showing enrichments for tumor cells, fibroblasts, and macrophages (Figure S7B), together forming 83.8% of cells in the EMT niche (Figure S7C). Therefore, we focused on these cell types to identify tumor-extrinsic molecular programs active in the EMT niche. Compatible with the LGALS1 function, myofibroblasts were not only the main enriched fibroblast state (Figure S7D), but their density actually peaked within the EMT niche compared with the rest of the tumor bed (Figure 7D). At the same time, macrophages in the EMT niche upregulated the expression of *SPP1* (secreted phosphoprotein-1 or osteopontin), together with the M2 marker

glutamine synthase (*GLUL*)⁵⁶ and the lipid-laden marker glycoprotein-NMB (*GPNMB*)⁵⁷ (Figure S7E), typical of tissue-repair and pro-tumoral macrophages.⁵⁸

Overall, the unbiased analysis of cell type-specific genes upregulated in the EMT niche revealed several key secreted molecules that have central roles in both wound healing and tumor invasion: *LGALS1* in tumor cells, *VEGFA* and *IGFBP5* in fibroblasts, and *SPP1* in macrophages. Suggesting their functional role in local tissue remodeling, their expression was not only enriched but almost spatially restricted to the EMT niche (Figures 7E–7G). For example, *VEGFA* promotes macrophage recruitment and their reprogramming toward an anti-inflammatory phenotype,⁵⁹ while insulin growth-factor-binding protein-5 (*IGFBP5*), especially in the presence of *FN1*,⁶⁰ promotes myofibroblast activation and ECM remodeling.⁶¹ Furthermore, *SPP1*+ macrophages have been recently identified as key

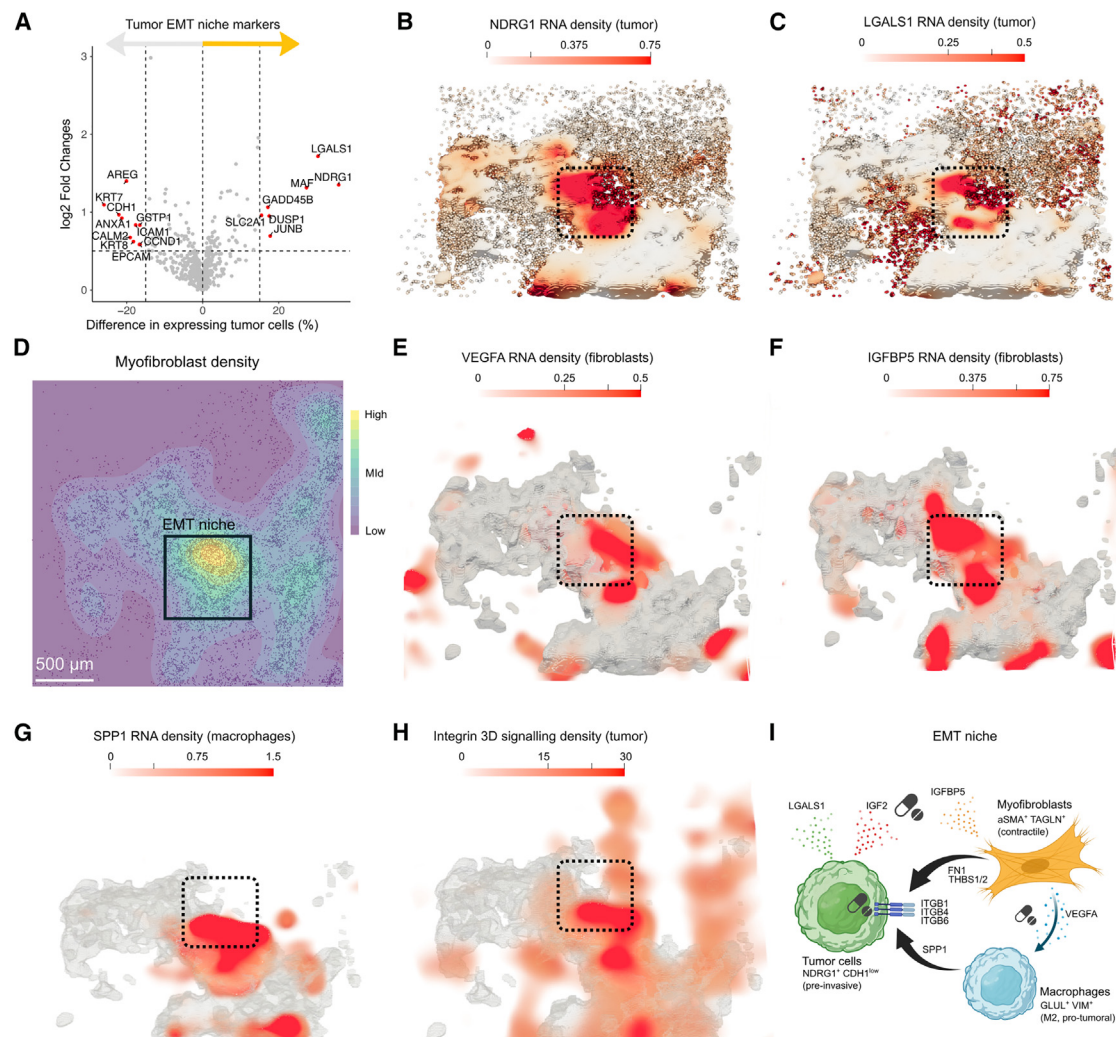


Figure 7. A wound healing-like, multicellular program activates integrin signaling in the EMT niche

(A) LGALS1 and NDRG1 expression characterizes tumor cells in the EMT niche. Scatter plot of differential gene expression in tumor cells inside vs. outside the EMT niche. x axis: difference in the percentage of expressing tumor cells. y axis: \log_2 fold changes of the average SCT-normalized tumor gene expression. Labeled: EMT niche differential tumor genes.

(B and C) NDRG1 (marker of brain metastasis) and LGALS1 (secreted during wound healing) expression is restricted to the tumor cells in the EMT niche (black box). 3D surface rendering of the gene expression density of EMT niche tumor marker genes.

(D) Myfibroblasts accumulate in the EMT niche. 3D spatial density plot of myfibroblasts.

(E and F) VEGFA (secreted in response to hypoxia and wound healing) and IGFBP5 (local regulator of IGF signaling) expression is restricted to fibroblasts in the EMT niche (black box). 3D surface rendering of the gene expression density of EMT niche fibroblast marker genes.

(G) SPP1 (secreted during wound healing) expression is restricted to macrophages in the EMT niche (black box). 3D surface rendering of the gene expression density of EMT niche macrophage marker gene.

(H) Tumor integrin signaling distinguishes the EMT from the rest of the tumor bed. 3D volumetric rendering of integrin signaling density, computed as the sum of all EMT niche-enriched interactions received by all tumor cells.

(I) A wound healing-like multicellular program characterizes the EMT niche and converges on the activation of integrin signaling. Summary scheme of selected cellular and molecular interactions in the EMT niche, revealing mechanism-based personalized targets for cancer interception. The pill symbol indicates druggable interactions.

players in myfibroblast recruitment and activation during tissue repair and fibrosis.⁶²

Finally, investigating which cell-cell interactions were received by tumor cells in the EMT niche, we identified 10 enriched interactions (Figure S7G) and mapped their multicellular communication networks (Figure S7H). Notably, all ligands (tumor: IGF2 and THBS1; macrophage: SPP1; and fibroblasts: FN1, THBS2,

COL1A2, and COL6A3) converged on the activation of tumor integrin receptors, namely ITGB1, ITGB4, and ITGB6.

Consistent with the hypothesis that tumors are “wounds that never heal,” often co-opting wound healing programs to promote tumor progression,⁶³ tumor cells in the EMT niche orchestrated the local recruitment and remodeling of fibroblast and macrophage phenotypes. In turn, given the central role of

integrin signaling in promoting tumor survival, EMT, and migration,⁴⁹ the convergence of myofibroblasts and SPP1+ macrophage-derived ligands on tumor integrin receptors provides a likely mechanism behind the accumulation of mesenchymal-like tumor cells in the EMT niche.

DISCUSSION

This study represents the proof-of-principle for the computational reconstruction and multimodal analysis of 3D cellular neighborhoods combining high-plex, single-cell resolved ST data with imaging readouts of the contextual ECM composition.

Overall, 3D neighborhoods captured how the TME is organized in multicellular niches and revealed niche-specific molecular mechanisms linking local cellular ecosystems and molecular states with receptor-ligand interactions. While 2D analysis of our data already captured most cellular niches, 3D neighborhoods improved the identification and characterization of immune niches in the patient under study. In line with the 3D multiplex IF study of one colorectal cancer sample,¹¹ 3D neighborhoods restored the spatial continuity of seemingly disconnected T cell niches in 2D. Furthermore, 3D analyses captured the spatial relationship between immune niches and the tumor surface and enabled the study of immune inhibitory interactions in dendritic cell niches.

At the same time, SHG highlighted the dynamic composition of the ECM in the TME, where the elastic lung ECM is degraded and progressively substituted by a stiff, desmoplastic ECM during tumor progression. The integrative analysis of gene expression and ECM remodeling was then instrumental in identifying which ECM constituents and regulators orchestrate local ECM metabolism and enabled the multimodal analysis of fibroblast molecular phenotypes in the TME. Notably, fibroblast phenotypes were spatially linked either with specific ECM compartments (e.g., activated fibroblasts in the desmoplastic ECM) or multicellular niches (e.g., CCL19+ fibroblasts in dendritic and T cell niches), supporting their functional specialization and organizing role in key local phenomena ranging from tumor invasion to anti-tumoral immune responses.

Finally, the spatial analysis of tumor pseudotime across multicellular niches and ECM compartments revealed how EMT was not restricted to tumor cells infiltrating a desmoplastic ECM but already occurred in one EMT niche at the tumor surface where a spatially restricted wound healing-like multicellular program induced pro-invasive integrin signaling⁶⁴ in a degraded ECM. In general, given the profound impact of tissue biomechanics in shaping cellular molecular states (and vice versa), we envision that the systematic integration of spatial mechanical and molecular readouts will reveal novel insights into tissue functioning in health and disease (e.g., shedding light on the intricate role of tumor-stromal interplay).

Focusing on an early-stage, aggressive NSCLC tumor, we showcase the power of our multimodal approach to pinpoint which, among multiple possible cancer progression mechanisms, are spatially linked with tumor invasion and immune escape in the patient under study. While a recent IMC study demonstrated how the TME spatial organization can accurately predict survival in early-stage NSCLC patients,⁶⁵ limited gene plex prevented the identification of personalized drug targets.

Here, leveraging the probe-based detection of receptor and ligand molecules (1–2 molecules/cell¹⁴) across neighboring cells, we boosted the sensitivity and specificity of our analysis compared with spatially agnostic expression of receptors and ligands in dissociated single cells. Our communication analysis identified which signaling axes could physically mediate key processes *in situ*. For example, Tregs and CTLs were recruited in hotspots of the tumor surface, where dendritic cells actively suppressed anti-tumor immunity through multiple immune checkpoints. Like the simultaneous identification of multiple druggable mutations by NGS sequencing opened the door to combination therapies,⁶⁶ we envision that the high-plex quantification of cell-cell interactions will pave the way to personalized therapies targeting the TME. For example, the combination of immune checkpoint inhibitors with small molecule inhibitors of intracellular integrin signaling (e.g., via FAK inhibitors⁶⁷) could represent a particularly attractive therapeutic strategy in the patient under study, simultaneously unleashing anti-tumoral immune responses and restraining tumor invasion.

Here we defined 3D neighborhoods using a 30 μm section-to-section gap as a cost-effective strategy to maximize 3D information while minimizing repeated sampling of the same cells (average cell radius 10–20 μm) and a neighborhood radius of 50 μm (~ 3 cellular distances) to capture repeating multicellular niches in this dataset. Nevertheless, the formal definition of cellular neighborhoods is still a matter of active research, and best practices are still lacking in the field, as the “optimal radius” is likely to be tissue, sample, cell, and analysis dependent. With the growing availability of 3D datasets, we expect that novel tools will facilitate the identification of the most appropriate neighborhood radius and section-to-section gap (e.g., to capture short vs. long-distance molecular dependencies). Moreover, rapid technological developments with increasing gene plex and/or resolution for unbiased spatial transcriptomic methods will enable the simultaneous profiling of ligand-receptor pairs together with intracellular response genes, further increasing the specificity of cell-cell communication analysis. At the same time, the rise of single-cell-resolved spatial proteomic methods⁶⁸ will further our understanding of local molecular mechanisms, enabling the study of protein abundances and post-translational modifications undetectable at the transcriptomic level.

Ultimately, our study provides the proof-of-principle for the integration of our high-plex assays compatible with routinely collected FFPE samples in molecular tumor boards (e.g., to inform N-of-One treatment of individual patients by treating physicians⁶⁹) and paves the way for large-scale clinical studies aimed at assessing the clinical benefit of mechanism-based, personalized therapeutic targets as those identified in this single-patient, observational study.

RESOURCE AVAILABILITY

Lead contact

Requests for further information should be directed and will be fulfilled by lead contact, Nikolaus Rajewsky (rajewsky@mdc-berlin.de).

Materials availability

This manuscript contains no unique reagents or resources. All antibodies and reagents are available commercially.

Data and code availability

- Raw and processed image-based ST and second harmonic imaging data generated in this study have been deposited at Zenodo (<https://doi.org/10.5281/zenodo.7899173>) and are publicly available as of the date of publication. Furthermore, it is possible to interactively explore the data in 3D through an interactive browser: <http://lung-3d-browser.mdc-berlin.de/>.
- This paper also analyzes existing, publicly available data. Accession numbers for all datasets are listed in the [key resources table](#).
- All original code has been deposited on Zenodo (<https://doi.org/10.5281/zenodo.7899173>) and GitHub (https://github.com/rajewsky-lab/3D_lung) and is publicly available as of the date of publication. Accession numbers are listed in the [key resource table](#).
- Any additional information required to reanalyze the data reported in this paper is available from the [lead contact](#) upon request.

ACKNOWLEDGMENTS

We thank Enes Senel, Marvin Jens, Leon Strenger, Kamil Lisek, Lieke van de Haar, Marie Schott, Cledi Alicia Cerda Jara, and all other members of the Rajewsky lab for critical and useful discussions. Alexandra Tschernycheff, Veronica Jakobi, and Margareta Herzog for the lab organizational support. We thank Anca Margineanu of the Advanced Light Microscopy Technology Platform at the Max-Delbrück-Center for her technical support with two-photon microscopy. A special thanks to Gaetano Gargiulo for reviewing the manuscript. N.R. and T.M.P. thank Nir Friedman for discussions and Stan Gorski for editorial feedback. The graphical abstract and illustrations in [Figures 1A, 4A, 4G, 7I, and S1A](#) were created with Biorender. T.M.P. is financially supported by the Berlin School of Integrative Oncology through the GSSP program of the German Academy of Exchange Service (DAAD) and by the Add-on Fellowship of the Joachim Herz Foundation. S.P. is supported by Fondazione AIRC under the “5 per mille 2019 – ID. 22759” program; the “Fondazione AIRC, IG 2019 ID. 23307 project”; and the ERC program CHARTAGING. M.C. is supported by Fondazione AIRC, IG 2022 ID. 27883 project. F.C., J.N., and S.F. acknowledge support by the Federal Ministry of Education and Research (BMBF), as part of the National Research Initiatives for mass spectrometry in systems medicine, under grant agreement no. 161L0222. N.R. thanks the Deutsche Forschungsgemeinschaft (DFG) grant number RA 838/5-1, Deutsches Zentrum für Herz-Kreislauf-Forschung (DZHK) grant numbers 81Z0100105 and 81X2100155, the Chan Zuckerberg Foundation (CZI)/Seed Network, and the NeuroCure/Cluster of Excellenz in the neurosciences at the Charité – Universitätsmedizin Berlin.

AUTHOR CONTRIBUTIONS

Conceptualization and design, T.M.P., I.L., N.K., and N.R.; methodology, T.M.P. and N.K.; sample collection and pathology analysis, S.S.; deep learning HE image analysis, S.S., L.R., and G.D.; sample processing and quality control, G.T. and A.B.; ST data collection and preprocessing, Y.K., S.K., S.M., and M.G.; second harmonic imaging data collection and preprocessing, A.W.; immunofluorescence data collection and preprocessing, D.L.-P., S.F., J.N., and P.J.; computational analysis, T.M.P. and N.K.; 3D renderings, D.L.-P.; writing – original draft, T.M.P.; writing – review & editing, T.M.P. and N.R. with input from I.T., I.L., M.C., S.P., F.C., N.K., and F.K. All authors discussed and analyzed the data.

DECLARATION OF INTERESTS

S.S. is an adviser for Aignostics. L.R. and G.D. are currently Aignostics employees. S.M., M.G., and Y.L. are current or past employees and shareholders of NanoString Technologies. F.K. is co-founder and adviser for Aignostics.

STAR★METHODS

Detailed methods are provided in the online version of this paper and include the following:

- **KEY RESOURCES TABLE**
- **EXPERIMENTAL MODEL AND SUBJECT DETAILS**
 - Human participants
- **METHOD DETAILS**
 - Study design
 - Sample collection and histological examination
 - Quantification of RNA fragmentation
 - CosMx sample processing, staining and imaging for 1000-plex RNA profiling
 - Second Harmonic Imaging (SHG)
 - Immunofluorescence (IF) imaging
 - Verhoef’s Van Gieson staining
- **QUANTIFICATION AND STATISTICAL ANALYSES**
 - Deep learning segmentation of whole slide H&E images
 - CosMx data processing
 - Unbiased transcriptomic clustering of segmented cells
 - Cell type annotation of transcriptomic clusters
 - Data integration with reference atlases
 - 3D alignment of spatial transcriptomic data
 - Identification of 2D and 3D cellular neighborhoods
 - Unbiased identification and annotation of 2D and 3D multicellular niches
 - Ligand spatial activity scores in 2D and 3D cellular neighborhoods
 - ECM composition analysis
 - Unbiased identification of ECM compartments
 - Fibroblast transcriptomic clustering and annotation
 - Tumor pseudotime analysis
 - Preprocessing of imaging data
 - Registration of IF and CosMx images
 - Niche enrichments
 - Quantification and visualization of 3D cellular density
 - 3D rendering of tissue niches, gene expression and ligand activity scores
 - Statistical methods

SUPPLEMENTAL INFORMATION

Supplemental information can be found online at <https://doi.org/10.1016/j.cels.2025.101261>.

Received: July 12, 2024

Revised: December 13, 2024

Accepted: March 19, 2025

Published: April 11, 2025

REFERENCES

1. Bejarano, L., Jordão, M.J.C., and Joyce, J.A. (2021). Therapeutic Targeting of the Tumor Microenvironment. *Cancer Discov.* **11**, 933–959. <https://doi.org/10.1158/2159-8290.CD-20-1808>.
2. Pickup, M.W., Mouw, J.K., and Weaver, V.M. (2014). The extracellular matrix modulates the hallmarks of cancer. *EMBO Rep.* **15**, 1243–1253. <https://doi.org/10.15252/EMBR.201439246>.
3. Joyce, J.A., and Pollard, J.W. (2009). Microenvironmental regulation of metastasis. *Nat. Rev. Cancer* **9**, 239–252. <https://doi.org/10.1038/NRC2618>.
4. Pardoll, D.M. (2012). The blockade of immune checkpoints in cancer immunotherapy. *Nat. Rev. Cancer* **12**, 252–264. <https://doi.org/10.1038/nrc3239>.
5. Chan, B.A., and Hughes, B.G.M. (2015). Targeted therapy for non-small cell lung cancer: current standards and the promise of the future. *Transl. Lung Cancer Res.* **4**, 36–54. <https://doi.org/10.3978/J.ISSN.2218-6751.2014.05.01>.
6. Reck, M., and Rabe, K.F. (2017). Precision Diagnosis and Treatment for Advanced Non–Small-Cell Lung Cancer. *N. Engl. J. Med.* **377**, 849–861. <https://doi.org/10.1056/NEJMra1703413>.

7. Torre, L.A., Bray, F., Siegel, R.L., Ferlay, J., Lortet-Tieulent, J., and Jemal, A. (2015). Global cancer statistics, 2012. *CA Cancer J. Clin.* 65, 87–108. <https://doi.org/10.3322/caac.21262>.
8. Robert, C. (2020). A decade of immune-checkpoint inhibitors in cancer therapy. *Nat. Commun.* 11, 3801. <https://doi.org/10.1038/s41467-020-17670-y>.
9. Davis-Marcisak, E.F., Deshpande, A., Stein-O'Brien, G.L., Ho, W.J., Laheru, D., Jaffee, E.M., Fertig, E.J., and Kagohara, L.T. (2021). From bench to bedside: Single-cell analysis for cancer immunotherapy. *Cancer Cell* 39, 1062–1080. <https://doi.org/10.1016/j.CCELL.2021.07.004>.
10. Kiemen, A.L., Braxton, A.M., Grahn, M.P., Han, K.S., Babu, J.M., Reichel, R., Jiang, A.C., Kim, B., Hsu, J., Amoa, F., et al. (2022). CODA: quantitative 3D reconstruction of large tissues at cellular resolution. *Nat. Methods* 19, 1490–1499. <https://doi.org/10.1038/s41592-022-01650-9>.
11. Lin, J.-R., Wang, S., Coy, S., Chen, Y.-A., Yapp, C., Tyler, M., Nariya, M.K., Heiser, C.N., Lau, K.S., Santagata, S., et al. (2023). Multiplexed 3D atlas of state transitions and immune interaction in colorectal cancer. *Cell* 186, 363–381.e19. <https://doi.org/10.1016/j.cell.2022.12.028>.
12. Kuett, L., Catena, R., Özcan, A., Plüss, A., Cancer Grand Challenges IMAXT Consortium, Schraml, P., Moch, H., de Souza, N., and Bodenmiller, B. (2022). Three-dimensional imaging mass cytometry for highly multiplexed molecular and cellular mapping of tissues and the tumor microenvironment. *Nat. Cancer* 3, 122–133. <https://doi.org/10.1038/s43018-021-00301-w>.
13. Palla, G., Fischer, D.S., Regev, A., and Theis, F.J. (2022). Spatial components of molecular tissue biology. *Nat. Biotechnol.* 40, 308–318. <https://doi.org/10.1038/s41587-021-01182-1>.
14. He, S., Bhatt, R., Brown, C., Brown, E.A., Buhr, D.L., Chantranuvatana, K., Danaher, P., Dunaway, D., Garrison, R.G., Geiss, G., et al. (2022). High-plex imaging of RNA and proteins at subcellular resolution in fixed tissue by spatial molecular imaging. *Nat. Biotechnol.* 40, 1794–1806. <https://doi.org/10.1038/s41587-022-01483-Z>.
15. Preibisch, S., Innerberger, M., León-Periñán, D., Karaiskos, N., and Rajewsky, N. (2025). Scalable image-based visualization and alignment of spatial transcriptomics datasets. *Cell Systems* 16, 101264. <https://doi.org/10.1016/j.cels.2025.101264>.
16. Travaglini, K.J., Nabhan, A.N., Penland, L., Sinha, R., Gillich, A., Sit, R.V., Chang, S., Conley, S.D., Mori, Y., Seita, J., et al. (2020). A molecular cell atlas of the human lung from single-cell RNA sequencing. *Nature* 587, 619–625. <https://doi.org/10.1038/s41586-020-2922-4>.
17. Kim, N., Kim, H.K., Lee, K., Hong, Y., Cho, J.H., Choi, J.W., Lee, J.I., Suh, Y.L., Ku, B.M., Eum, H.H., et al. (2020). Single-cell RNA sequencing demonstrates the molecular and cellular reprogramming of metastatic lung adenocarcinoma. *Nat. Commun.* 11, 2285. <https://doi.org/10.1038/s41467-020-16164-1>.
18. Zhou, J., Kulasinghe, A., Bogseth, A., O'Byrne, K., Punyadeera, C., and Papautsky, I. (2019). Isolation of circulating tumor cells in non-small-cell-lung-cancer patients using a multi-flow microfluidic channel. *Microsyst. Nanoeng.* 5, 8. <https://doi.org/10.1038/s41378-019-0045-6>.
19. Sikkema, L., Ramírez-Suástegui, C., Strobl, D.C., Gillett, T.E., Zappia, L., Madissoon, E., Markov, N.S., Zaragosi, L.E., Ji, Y., Ansari, M., et al. (2023). An integrated cell atlas of the lung in health and disease. *Nat. Med.* 29, 1563–1577. <https://doi.org/10.1038/s41591-023-02327-2>.
20. Jin, S., Guerrero-Juarez, C.F., Zhang, L., Chang, I., Ramos, R., Kuan, C.H., Myung, P., Plikus, M.V., and Nie, Q. (2021). Inference and analysis of cell-cell communication using CellChat. *Nat. Commun.* 12, 1088. <https://doi.org/10.1038/s41467-021-21246-9>.
21. Schall, T.J., Bacon, K., Toy, K.J., and Goeddel, D.V. (1990). Selective attraction of monocytes and T lymphocytes of the memory phenotype by cytokine RANTES. *Nature* 347, 669–671. <https://doi.org/10.1038/347669A0>.
22. Förster, R., Davalos-Misslitz, A.C., and Rot, A. (2008). CCR7 and its ligands: balancing immunity and tolerance. *Nat. Rev. Immunol.* 8, 362–371. <https://doi.org/10.1038/NRI2297>.
23. Wculek, S.K., Cueto, F.J., Mujal, A.M., Melero, I., Krummel, M.F., and Sancho, D. (2020). Dendritic cells in cancer immunology and immunotherapy. *Nat. Rev. Immunol.* 20, 7–24. <https://doi.org/10.1038/s41577-019-0210-Z>.
24. Chen, J.H., Nieman, L.T., Spurrell, M., Jorgji, V., Richieri, P., Xu, K.H., Madhu, R., Parikh, M., Zamora, I., Mehta, A., et al. (2023). Spatial analysis of human lung cancer reveals organized immune hubs enriched for stem-like CD8 T cells and associated with immunotherapy response. Preprint at bioRxiv. <https://doi.org/10.1101/2023.04.04.535379>.
25. Mora Barthelmess, R., Stijlemans, B., and Van Ginderachter, J.A. (2023). Hallmarks of Cancer Affected by the MIF Cytokine Family. *Cancers (Basel)* 15, 395. <https://doi.org/10.3390/CANCERS15020395>.
26. Figueiredo, C.R., Azevedo, R.A., Mousdell, S., Resende-Lara, P.T., Ireland, L., Santos, A., Girola, N., Cunha, R.L.O.R., Schmid, M.C., Polonelli, L., et al. (2018). Blockade of MIF-CD74 signalling on macrophages and dendritic cells restores the antitumour immune response against metastatic melanoma. *Front. Immunol.* 9, 1132. <https://doi.org/10.3389/fimmu.2018.01132>.
27. Keren, L., Bosse, M., Marquez, D., Angoshtari, R., Jain, S., Varma, S., Yang, S.R., Kurian, A., Van Valen, D., West, R., et al. (2018). A Structured Tumor-Immune Microenvironment in Triple Negative Breast Cancer Revealed by Multiplexed Ion Beam Imaging. *Cell* 174, 1373–1387.e19. <https://doi.org/10.1016/j.cell.2018.08.039>.
28. Herbst, R.S., Soria, J.C., Kowanzet, M., Fine, G.D., Hamid, O., Gordon, M.S., Sosman, J.A., McDermott, D.F., Powderly, J.D., Gettinger, S.N., et al. (2014). Predictive correlates of response to the anti-PD-L1 antibody MPDL3280A in cancer patients. *Nature* 515, 563–567. <https://doi.org/10.1038/nature14011>.
29. Hynes, R.O. (2009). The Extracellular Matrix: Not Just Pretty Fibrils. *Science* 326, 1216–1219. <https://doi.org/10.1126/SCIENCE.1176009>.
30. Dunsmore, S.E., and Rannels, D.E. (1996). Extracellular matrix biology in the lung. *Am. J. Physiol.* 270, L3–27. <https://doi.org/10.1152/ajplung.1996.270.1.L3>.
31. Chen, X., Nadiarynk, O., Plotnikov, S., and Campagnola, P.J. (2012). Second harmonic generation microscopy for quantitative analysis of collagen fibrillar structure. *Nat. Protoc.* 7, 654–669. <https://doi.org/10.1038/nprot.2012.009>.
32. Prêle, C.M., Miles, T., Pearce, D.R., O'Donoghue, R.J., Grainge, C., Barrett, L., Birnie, K., Lucas, A.D., Baltic, S., Ernst, M., et al. (2022). Plasma cell but not CD20-mediated B-cell depletion protects from bleomycin-induced lung fibrosis. *Eur. Respir. J.* 60, 2101469. <https://doi.org/10.1183/13993003.01469-2021>.
33. Kai, F., Drain, A.P., and Weaver, V.M. (2019). The Extracellular Matrix Modulates the Metastatic Journey. *Dev. Cell* 49, 332–346. <https://doi.org/10.1016/j.devcel.2019.03.026>.
34. DeLeon-Pennell, K.Y., Barker, T.H., and Lindsey, M.L. (2020). Fibroblasts: The arbiters of extracellular matrix remodeling. *Matrix Biol.* 91–92, 1–7. <https://doi.org/10.1016/j.MATBIO.2020.05.006>.
35. Kalluri, R., and Zeisberg, M. (2006). Fibroblasts in cancer. *Nat. Rev. Cancer* 6, 392–401. <https://doi.org/10.1038/nrc1877>.
36. Chhabra, Y., and Weeraratna, A.T. (2023). Fibroblasts in cancer: Unity in heterogeneity. *Cell* 186, 1580–1609. <https://doi.org/10.1016/j.CELL.2023.03.016>.
37. Sahai, E., Astsaturov, I., Cukierman, E., DeNardo, D.G., Egeblad, M., Evans, R.M., Fearon, D., Gretchen, F.R., Hingorani, S.R., Hunter, T., et al. (2020). A framework for advancing our understanding of cancer-associated fibroblasts. *Nat. Rev. Cancer* 20, 174–186. <https://doi.org/10.1038/s41568-019-0238-1>.
38. Naba, A., Clauser, K.R., Ding, H., Whittaker, C.A., Carr, S.A., and Hynes, R.O. (2016). The extracellular matrix: Tools and insights for the “omics” era. *Matrix Biol.* 49, 10–24. <https://doi.org/10.1016/j.MATBIO.2015.06.003>.
39. Ansorge, H.L., Meng, X., Zhang, G., Veit, G., Sun, M., Klement, J.F., Beason, D.P., Soslowsky, L.J., Koch, M., and Birk, D.E. (2009). Type XIV

- Collagen Regulates Fibrillogenesis: PREMATURE COLLAGEN FIBRIL GROWTH AND TISSUE DYSFUNCTION IN NULL MICE. *J. Biol. Chem.* 284, 8427–8438. <https://doi.org/10.1074/jbc.M805582200>.
40. Hynes, R.O. (1990). *Fibronectins* (Springer). <https://doi.org/10.1007/978-1-4612-3264-3>.
41. Vázquez-Villa, F., García-Ocaña, M., Galván, J.A., García-Martínez, J., García-Pravia, C., Menéndez-Rodríguez, P., González-del Rey, C.G. del Barneo-Serra, L., and de los Toyos, J.R. (2015). COL11A1/(pro)collagen 11A1 expression is a remarkable biomarker of human invasive carcinoma-associated stromal cells and carcinoma progression. *Tumour Biol.* 36, 2213–2222. <https://doi.org/10.1007/S13277-015-3295-4>.
42. Moore, C.S., and Crocker, S.J. (2012). An Alternate Perspective on the Roles of TIMPs and MMPs in Pathology. *Am. J. Pathol.* 180, 12–16. <https://doi.org/10.1016/j.ajpath.2011.09.008>.
43. Zheng, N., Wen, R., Zhou, L., Meng, Q., Zheng, K., Li, Z., Cao, F., and Zhang, W. (2023). Multiregion single cell analysis reveals a novel subtype of cancer-associated fibroblasts located in the hypoxic tumor microenvironment in colorectal cancer. *Transl. Oncol.* 27, 101570. <https://doi.org/10.1016/J.TRANON.2022.101570>.
44. Wittekind, C., and Neid, M. (2005). Cancer invasion and metastasis. *Oncology* 69, 14–16. <https://doi.org/10.1159/000086626>.
45. Yang, J., Antin, P., Berx, G., Blanpain, C., Brabletz, T., Bronner, M., Campbell, K., Cano, A., Casanova, J., Christofori, G., et al. (2020). Guidelines and definitions for research on epithelial–mesenchymal transition. *Nat. Rev. Mol. Cell Biol.* 21, 341–352. <https://doi.org/10.1038/s41580-020-0237-9>.
46. Wei, S.C., Fattet, L., Tsai, J.H., Guo, Y., Pai, V.H., Majeski, H.E., Chen, A.C., Sah, R.L., Taylor, S.S., Engler, A.J., et al. (2015). Matrix stiffness drives epithelial–mesenchymal transition and tumour metastasis through a TWIST1–G3BP2 mechanotransduction pathway. *Nat. Cell Biol.* 17, 678–688. <https://doi.org/10.1038/NCB3157>.
47. Down-Regulation of E-Cadherin Gene Expression by Collagen Type I and Type III in Pancreatic Cancer Cell Lines1 | Cancer Research (American Association for Cancer Research). <https://aacrjournals.org/cancerres/article/61/8/3508/508645/Down-Regulation-of-E-Cadherin-Gene-Expression-by>.
48. Panciera, T., Citron, A., Di Biagio, D., Battilana, G., Gandin, A., Giullitti, S., Forcato, M., Biciato, S., Panzetta, V., Fusco, S., et al. (2020). Reprogramming normal cells into tumour precursors requires ECM stiffness and oncogene-mediated changes of cell mechanical properties. *Nat. Mater.* 19, 797–806. <https://doi.org/10.1038/s41563-020-0615-x>.
49. Hamidi, H., and Ivaska, J. (2018). Every step of the way: integrins in cancer progression and metastasis. *Nat. Rev. Cancer* 18, 533–548. <https://doi.org/10.1038/s41568-018-0038-z>.
50. Lo, C.M., Wang, H.B., Dembo, M., and Wang, Y.L. (2000). Cell Movement Is Guided by the Rigidity of the Substrate. *Biophys. J.* 79, 144–152. [https://doi.org/10.1016/S0006-3495\(00\)76279-5](https://doi.org/10.1016/S0006-3495(00)76279-5).
51. Rajewsky, N., Almouzni, G., Gorski, S.A., Aerts, S., Amit, I., Bertero, M.G., Bock, C., Bredenoord, A.L., Cavalli, G., Chiocca, S., et al. (2020). LifeTime and improving European healthcare through cell-based interceptive medicine. *Nature* 587, 377–386. <https://doi.org/10.1038/s41586-020-2715-9>.
52. Wang, Y., Zhou, Y., Tao, F., Chai, S., Xu, X., Yang, Y., Yang, Y., Xu, H., and Wang, K. (2017). N-myc downstream regulated gene 1 (NDRG1) promotes the stem-like properties of lung cancer cells through stabilized c-Myc. *Cancer Lett.* 401, 53–62. <https://doi.org/10.1016/J.CANLET.2017.04.031>.
53. Zhang, Q., Abdo, R., Iosef, C., Kaneko, T., Cecchini, M., Han, V.K., and Li, S.S.C. (2022). The spatial transcriptomic landscape of non-small cell lung cancer brain metastasis. *Nat. Commun.* 13, 5983. <https://doi.org/10.1038/S41467-022-33365-Y>.
54. Sundblad, V., Morosi, L.G., Geffner, J.R., and Rabinovich, G.A. (2017). Galectin-1: A Jack-of-All-Trades in the Resolution of Acute and Chronic Inflammation. *J. Immunol.* 199, 3721–3730. <https://doi.org/10.4049/JIMMUNOL.1701172>.
55. Lin, Y.T., Chen, J.S., Wu, M.H., Hsieh, I.S., Liang, C.H., Hsu, C.L., Hong, T.M., and Chen, Y.L. (2015). Galectin-1 Accelerates Wound Healing by Regulating the Neuropilin-1/Smad3/NOX4 Pathway and ROS Production in Myofibroblasts. *J. Invest. Dermatol.* 135, 258–268. <https://doi.org/10.1038/JID.2014.288>.
56. Palmieri, E.M., Menga, A., Martín-Pérez, R., Quinto, A., Riera-Domingo, C., De Tullio, G., Hooper, D.C., Lamers, W.H., Ghesquière, B., McVicar, D.W., et al. (2017). Pharmacologic or Genetic Targeting of Glutamine Synthetase Skews Macrophages toward an M1-like Phenotype and Inhibits Tumor Metastasis. *Cell Rep.* 20, 1654–1666. <https://doi.org/10.1016/j.celrep.2017.07.054>.
57. van Eijk, M., and Aerts, J.M.F.G. (2021). The Unique Phenotype of Lipid-Laden Macrophages. *Int. J. Mol. Sci.* 22, 4039. <https://doi.org/10.3390/IJMS22084039>.
58. Mantovani, A., Sozzani, S., Locati, M., Allavena, P., and Sica, A. (2002). Macrophage polarization: Tumor-associated macrophages as a paradigm for polarized M2 mononuclear phagocytes. *Trends Immunol.* 23, 549–555. [https://doi.org/10.1016/S1471-4906\(02\)02302-5](https://doi.org/10.1016/S1471-4906(02)02302-5).
59. Ohm, J.E., Gabrilovich, D.I., Sempowski, G.D., Kisseleva, E., Parman, K.S., Nadaf, S., and Carbone, D.P. (2003). VEGF inhibits T-cell development and may contribute to tumor-induced immune suppression. *Blood* 101, 4878–4886. <https://doi.org/10.1182/blood-2002-07-1956>.
60. Jones, J.I., Gockerman, A., Busby, W.H., Camacho-Hubner, C., and Clemmons, D.R. (1993). Extracellular matrix contains insulin-like growth factor binding protein-5: potentiation of the effects of IGF-I. *J. Cell Biol.* 121, 679–687. <https://doi.org/10.1083/JCB.121.3.679>.
61. Wang, W., Li, P., Li, W., Jiang, J., Cui, Y., Li, S., and Wang, Z. (2017). Osteopontin activates mesenchymal stem cells to repair skin wound. *PLoS One* 12, e0185346. <https://doi.org/10.1371/JOURNAL.PONE.0185346>.
62. Hoefft, K., Schaefer, G.J.L., Kim, H., Schumacher, D., Bleckwehl, T., Long, Q., Klinkhammer, B.M., Peisker, F., Koch, L., Nagai, J., et al. (2023). Platelet-instructed SPP1+ macrophages drive myofibroblast activation in fibrosis in a CXCL4-dependent manner. *Cell Rep.* 42, 112131. <https://doi.org/10.1016/j.celrep.2023.112131>.
63. Flier, J.S., Underhill, L.H., and Dvorak, H.F. (1986). Tumors: Wounds That Do Not Heal. *N. Engl. J. Med.* 315, 1650–1659. <https://doi.org/10.1056/NEJM198612253152606>.
64. Levental, K.R., Yu, H., Kass, L., Lakins, J.N., Egeblad, M., Erler, J.T., Fong, S.F.T., Csiszar, K., Giaccia, A., Weninger, W., et al. (2009). Matrix cross-linking forces tumor progression by enhancing integrin signaling. *Cell* 139, 891–906. <https://doi.org/10.1016/J.CELL.2009.10.027>.
65. Sorin, M., Rezanejad, M., Karimi, E., Fiset, B., Desharnais, L., Perus, L.J.M., Milette, S., Yu, M.W., Maritan, S.M., Doré, S., et al. (2023). Single-cell spatial landscapes of the lung tumour immune microenvironment. *Nature* 614, 548–554. <https://doi.org/10.1038/s41586-022-05672-3>.
66. Dietel, M., and Sers, C. (2006). Personalized medicine and development of targeted therapies: The upcoming challenge for diagnostic molecular pathology. A review. *Virchows Arch.* 448, 744–755. <https://doi.org/10.1007/S00428-006-0189-2>.
67. Golubovskaya, V.M. (2014). Targeting FAK in human cancer: from finding to first clinical trials. *Front. Biosci. (Landmark Ed.)* 19, 687–706. <https://doi.org/10.2741/4236>.
68. Mund, A., Coscia, F., Kriston, A., Hollandi, R., Kovács, F., Brunner, A.D., Migh, E., Schweizer, L., Santos, A., Bzorek, M., et al. (2022). Deep Visual Proteomics defines single-cell identity and heterogeneity. *Nat. Biotechnol.* 40, 1231–1240. <https://doi.org/10.1038/s41587-022-01302-5>.
69. Kato, S., Kim, K.H., Lim, H.J., Boichard, A., Nikanjam, M., Weihe, E., Kuo, D.J., Eskander, R.N., Goodman, A., Galanina, N., et al. (2020). Real-world data from a molecular tumor board demonstrates improved outcomes with a precision N-of-One strategy. *Nat. Commun.* 11, 4965. <https://doi.org/10.1038/s41467-020-18613-3>.

70. Stringer, C., Wang, T., Michaelos, M., and Pachitariu, M. (2021). Cellpose: a generalist algorithm for cellular segmentation. *Nat. Methods* 18, 100–106. <https://doi.org/10.1038/S41592-020-01018-X>.
71. Stuart, T., Butler, A., Hoffman, P., Hafemeister, C., Papalexi, E., Mauck, W.M., Hao, Y., Stoeckius, M., Smibert, P., and Satija, R. (2019). Comprehensive Integration of Single-Cell Data. *Cell* 177, 1888–1902.e21. <https://doi.org/10.1016/j.cell.2019.05.031>.
72. Amezquita, R.A., Lun, A.T.L., Becht, E., Carey, V.J., Carpp, L.N., Geistlinger, L., Marini, F., Rue-Albrecht, K., Risso, D., Sonesson, C., et al. (2020). Orchestrating single-cell analysis with Bioconductor. *Nat. Methods* 17, 137–145. <https://doi.org/10.1038/s41592-019-0654-x>.
73. Ahrens, J., Geveci, B., and Law, C. (2005). ParaView: An End-User Tool for Large-Data Visualization. In *Visualization Handbook* (Elsevier), pp. 717–731. <https://doi.org/10.1016/B978-012387582-2/50038-1>.
74. Preibisch, S., Saalfeld, S., and Tomancak, P. (2009). Globally optimal stitching of tiled 3D microscopic image acquisitions. *Bioinformatics* 25, 1463–1465. <https://doi.org/10.1093/BIOINFORMATICS/BTP184>.
75. Eng, J., Bucher, E., Hu, Z., Zheng, T., Gibbs, S.L., Chin, K., and Gray, J.W. (2022). A framework for multiplex imaging optimization and reproducible analysis. *Commun. Biol.* 5, 438. <https://doi.org/10.1038/S42003-022-03368-Y>.
76. Weng, W., and Zhu, X. (2015). U-Net: Convolutional Networks for Biomedical Image Segmentation. *IEEE Access* 9, 16591–16603. <https://doi.org/10.48550/arxiv.1505.04597>.
77. He, K., Zhang, X., Ren, S., and Sun, J. (2016). Deep Residual Learning for Image Recognition. In 2016 IEEE Conference on Computer Vision and Pattern Recognition (CVPR) (IEEE), pp. 770–778. <https://doi.org/10.1109/CVPR.2016.90>.
78. Kingma, D.P., and Ba, J.L. (2014). Adam: A Method for Stochastic. In 3rd International Conference on Learning Representations (ICLR 2015). <https://doi.org/10.48550/arxiv.1412.6980>.
79. Hafemeister, C., and Satija, R. (2019). Normalization and variance stabilization of single-cell RNA-seq data using regularized negative binomial regression. *Genome Biol.* 20, 296. <https://doi.org/10.1186/s13059-019-1874-1>.
80. McInnes, L., Healy, J., Saul, N., and Großberger, L. (2018). UMAP: Uniform Manifold Approximation and Projection. *J. Open Source Softw.* 3, 861. <https://doi.org/10.21105/JOSS.00861>.
81. Lowe, D.G. (1999). Object recognition from local scale-invariant features. In *Proceedings of the IEEE International Conference on Computer Vision 2 (IEEE)*, pp. 1150–1157. <https://doi.org/10.1109/ICCV.1999.790410>.
82. Kieffer, Y., Hocine, H.R., Gentric, G., Pelon, F., Bernard, C., Bourachot, B., Lameiras, S., Albergante, L., Bonneau, C., Guyard, A., et al. (2020). Single-cell analysis reveals fibroblast clusters linked to immunotherapy resistance in cancer. *Cancer Discov.* 10, 1330–1351. <https://doi.org/10.1158/2159-8290.CD-19-1384>.
83. Lambrechts, D., Wauters, E., Boeckx, B., Aibar, S., Nittner, D., Burton, O., Bassez, A., Decaluwé, H., Pircher, A., Van den Eynde, K., et al. (2018). Phenotype molding of stromal cells in the lung tumor microenvironment. *Nat. Med.* 24, 1277–1289. <https://doi.org/10.1038/S41591-018-0096-5>.
84. Elyada, E., Bolisetty, M., Laise, P., Flynn, W.F., Courtois, E.T., Burkhart, R.A., Teinor, J.A., Belleau, P., Biffi, G., Lucito, M.S., et al. (2019). Cross-Species Single-Cell Analysis of Pancreatic Ductal Adenocarcinoma Reveals Antigen-Presenting Cancer-Associated Fibroblasts. *Cancer Discov.* 9, 1102–1123. <https://doi.org/10.1158/2159-8290.CD-19-0094>.
85. Fletcher, A.L., Acton, S.E., and Knoblich, K. (2015). Lymph node fibroblastic reticular cells in health and disease. *Nat. Rev. Immunol.* 15, 350–361. <https://doi.org/10.1038/NRI3846>.
86. Cords, L., Tietscher, S., Anzeneder, T., Langwieder, C., Rees, M., Souza, N. de, and Bodenmiller, B. (2022). A Cancer-Associated Fibroblast Classification Framework for Single-Cell Data. Preprint at bioRxiv. <https://doi.org/10.1101/2022.12.14.520398>.
87. Street, K., Risso, D., Fletcher, R.B., Das, D., Ngai, J., Yosef, N., Purdom, E., and Dudoit, S. (2018). Slingshot: Cell lineage and pseudotime inference for single-cell transcriptomics. *BMC Genomics* 19, 477. <https://doi.org/10.1186/s12864-018-4772-0>.
88. Muhlich, J.L., Chen, Y.-A., Yapp, C., Russell, D., Santagata, S., and Sorger, P.K. (2022). Stitching and registering highly multiplexed whole-slide images of tissues and tumors using ASHLAR. *Bioinformatics* 38, 4613–4621. <https://doi.org/10.1093/BIOINFORMATICS/BTAC544>.
89. Linkert, M., Rueden, C.T., Allan, C., Burel, J.M., Moore, W., Patterson, A., Loranger, B., Moore, J., Neves, C., MacDonald, D., et al. (2010). Metadata matters: access to image data in the real world. *J. Cell Biol.* 189, 777–782. <https://doi.org/10.1083/JCB.201004104>.

STAR★METHODS

KEY RESOURCES TABLE

REAGENT or RESOURCE	SOURCE	IDENTIFIER
Antibodies		
Anti-E-Cadherin [24E10] (Alexa Fluor(R) 488)	Cell Signaling Technology	RRID: AB_10691457
Anti-Pan-Cytokeratin [AE1/AE3] (eFluor 570)	Thermo Fisher Scientific	RRID: AB_11218704
Anti-CD68 (D4B9C) XP® (PE Conjugate)	Cell Signaling Technology	RRID: AB_2799935
Anti-Indoleamine 2, 3-dioxygenase [EPR20374] (Alexa Fluor® 647)	Abcam	RRID: AB_2943198
Biological samples		
Human non-small cell lung cancer tissue (FFPE)	Institute of Pathology, Charité Universitätsmedizin Berlin	N/A
Chemicals, peptides, and recombinant proteins		
Hematoxylin solution A acc. to Weigert	Carl Roth	Art. No. X906.1
Hematoxylin solution B acc. to Weigert	Carl Roth	Art. No. X907.1
Van Gieson's Solution	Carl Roth	Art. No. 3925.1
Critical commercial assays		
CosMx Spatial Molecular Imager (1000-plex)	NanoString Technologies	https://nanosttring.com/products/cosmx-spatial-molecular-imager/
Deposited data		
CosMx data	This study	https://doi.org/10.5281/zenodo.7899173
SHG data	This study	https://doi.org/10.5281/zenodo.7899173
Healthy lung cell atlas from Travaglini et al ¹⁷	Synapse	syn21041850
NSCLC single cell data from Kim et al ¹⁹	GEO	GSE131907
Software and algorithms		
Cellpose	Stringer et al ⁷⁰	https://github.com/MouseLand/cellpose
Seurat v4.0.4	Stuart et al ⁷¹	https://satijalab.org/seurat/
STIM v 0.2.0	Preibisch et al ¹⁵	https://github.com/PreibischLab/STIM
Slingshot v2.2.1	Street et al ⁷²	https://github.com/kstreet13/slinsshot
ParaView v 5.10	Ahrens et al. ⁷³	https://www.paraview.org/
Fiji v 1.53t	Preibisch et al ⁷⁴	https://imagej.net/software/fiji/
CellChat	Jin et al ²⁰	http://www.cellchat.org/
Others		
Interactive 3D browser	This study	https://lung-3d-browser.mdc-berlin.de
Code to reproduce results and figures	This study	https://github.com/rajewsky-lab/3D_lung

EXPERIMENTAL MODEL AND SUBJECT DETAILS

Human participants

One non-small cell lung cancer tumor obtained through lobectomy was included in the study. The patient was a 63-year-old female, who presented with a pulmonary tumor mass in the apex of the right upper lobe (RUL) in the positron emission tomography in March 2020. The patient was a 40 pack-year ex-smoker, fully active and without any physical restrictions (ECOG grade 0). A transbronchial lung biopsy revealed a TTF1-positive lung adenocarcinoma (LUAD) with acinar morphology. Staging workup by abdominal and a brain CT-scan showed no other potential lesions, additionally the bone scintigraphy was negative. Two months after initial diagnosis, a resection of the RUL was performed. The pathological examination revealed a tumor with a maximum diameter of 23 mm, infiltration of the visceral pleura, lymphovascular invasion, and three metastases into hilar lymph nodes with a maximum diameter of 7 mm. The tumor was completely resected. The pathological tumor classification was as follows: pT2a pN1 (3/24) L1 V0 Pn0 G2 R0. The patient received three cycles of an adjuvant-combined chemotherapy (Cisplatin + Vinorelbine). In February 2021, the patient started having neuronal symptoms and a magnetic resonance tomography of the head was performed revealing a 10 mm tumor in the frontal cortex. The tumor was resected and a metastasis of the LUAD was histologically confirmed. Afterwards the patient received cranial

radiotherapy in the form of a volumetric intensity modulated arc therapy (VMAT) at a dosage of 25,6 Gray (Gy). In August 2021 a second metastasis was diagnosed in the left upper lobe (LUL) of the lung.

METHOD DETAILS

Study design

To study three-dimensional (3D) cellular neighborhoods in the tumor microenvironment (TME), we focused on a formalin-fixed, paraffin-embedded (FFPE) tumor block from a NSCLC patient and collected 34 5 μm -thick consecutive sections using a microtome. We processed sections 4, 10, 16, 22, 28 and 34 with CosMx (section-to-section distance 30 μm) to generate high-plex, single-cell resolved spatial transcriptomics data, section 3 with both second harmonic imaging (SHG) to study extracellular matrix (ECM) composition and hematoxylin and eosin (H&E) staining to capture tissue morphology and section 12 with immunofluorescence (IF) to validate tumor epithelial-to-mesenchymal transition (EMT) at the protein level. We then employed computational methods for the 3D alignment of the analyzed sections to generate a 3D multimodal atlas of NSCLC at single cell resolution.

Sample collection and histological examination

Resected specimens and core needle biopsies were fixed in 10% buffered formalin before gross processing. After overnight fixation, the specimens were cut in 5-mm-thick slices. As a first step, the tumor was detected, described and the tumor diameter as well as the minimum distances to the visceral pleura and the resection margins of lung parenchyma and bronchus were measured. Next, the resection margins and the representative tumor parts showing the relation to the relevant anatomical structures, described above, were embedded. Furthermore, we retrieved all macroscopic detectable lymph nodes. Subsequently the tissue or biopsies were embedded in paraffin and were stored at room temperature at the archive of the Institute of Pathology at the Charité University Hospital, Campus Mitte. Histological examination, including diagnosis, tumor grading, pTNM-classification, angioinvasion, lymphatic invasion, and tumor stage was done according to the 8th edition of the TNM classification (AJCC). The study was performed according to the ethical principles for medical research of the Declaration of Helsinki and approval was approved by the Ethics Committee of the Charité University Medical Department in Berlin (EA4/243/21).

Quantification of RNA fragmentation

To quantify the extent of RNA fragmentation, we collected 3 10 μm sections using a Microtome (Leica Byostems). We then extracted RNA using Qiagen RNAse FFPE kit according to manufacturer instructions and evaluated the percentage of total RNA fragments longer than 200 nucleotides (DV200) using the TapeStation (Agilent). Compatible with formalin fixation and prolonged storage at room temperature, the DV200 score was 60%.

CosMx sample processing, staining and imaging for 1000-plex RNA profiling

CosMx sample processing, staining, imaging, and cell segmentation were performed as previously described.¹⁴ Briefly, tissue sections were placed to VWR Superfrost Plus Micro Slide (Cat# 48311-703) for optimal adherence. Slides were then dried at 37°C overnight, followed by deparaffinization, antigen retrieval and proteinase mediated permeabilization (<https://nanosttring.com/products/cosmx-spatial-molecular-imager/single-cell-imaging-overview/>). 1 nM RNA-ISH probes were applied for hybridization at 37°C overnight. After stringent wash, a flow cell was assembled on top of the slide and cyclic RNA readout on CosMx was performed (16-digit encoding strategy). After all cycles were completed, additional visualization markers for morphology and cell segmentation were added including pan-cytokeratin, CD45, CD3, CD298/B2M, and DAPI. Twenty-four 0.985mm \times 0.657mm fields of view (FOVs) were selected for data collection in each slice. The CosMx optical system has an epifluorescent configuration based on a customized water objective (13 \times , NA 0.82), and uses widefield illumination, with a mix of lasers and light-emitting diodes (385 nm, 488 nm, 530 nm, 590 nm, 647 nm) that allow imaging of DAPI, Alexa Fluor-488, Atto-532, Dyomics Dy-605 and Alexa Fluor-647, as well as removal of photocleavable dye components. The camera was a FLIR BFS-U3_200S6M-C based on the IMX183 Sony industrial CMOS sensor (pixel size 180nm). A 3D multichannel image stack (9 frames) was obtained at each FOV location, with the step size of 0.8 μm .

Second Harmonic Imaging (SHG)

Label free imaging of collagen and elastin was performed on a Zeiss LSM 880 NLO equipped with a Plan-Apochromat 10x NA 0.45 objective (Carl Zeiss Microscopy GmbH, Jena, Germany) and a tunable femtosecond titanium-sapphire laser (Chameleon-Ultra II, Coherent, Santa Clara, California). Using an excitation wavelength of 800 nm, the second-harmonic generation signal from collagen was collected through a 395 – 405 nm spectral window on to a GaAsP detector and autofluorescence emission from elastin was collected through a 435 – 480 nm spectral window on to a PMT.

Immunofluorescence (IF) imaging

The IF workflow for FFPE tissues was performed as previously described.⁷⁵ In detail, FFPE tissue was deparaffinized, rehydrated and a two-step antigen retrieval was performed at pH 6 and pH 9 sequentially with a rinsing step in PBS in between. Slides were blocked in Odyssey blocking buffer (LI-COR BioScience, Cat # 927-70001) for 30 minutes. Prior to antibody incubation, a pre-bleaching step was performed in 4.5% H_2O_2 and 24 mM NaOH diluted in PBS for 30 minutes at room temperature in the presence of white light.

The tissue was counterstained with Hoechst 33342 (Thermo Fisher Scientific, Cat #62249), mounted with ProLong™ Diamond (Thermo Fisher Scientific, Cat #P36961) and imaged. After acquisition, slides were soaked in PBS for 5–10 minutes to remove the coverslip and antibody incubation was performed in a humid chamber at 4 °C overnight. Slides were then washed, mounted, imaged and bleached. Images were acquired on a Zeiss AxioScan7 Slide scanner using an EC Plan-Neofluor 20x/0.5 M27 objective with 1x1 binning.

Verhoef's Van Gieson staining

Paraffin was removed using xylene, and the slides were rehydrated through graded ethanol solutions to distilled water. Elastic fibers were stained using freshly prepared Weigert's Resorcin-Fuchsin solution. The staining solution was prepared by mixing Weigert's Solution A (Carl Roth, Karlsruhe, Germany) with Weigert's Solution B (Carl Roth GmbH, Karlsruhe, Germany) in appropriate proportions according to the manufacturer's instructions. The slides were incubated in this solution for 10–15 minutes at room temperature to ensure clear staining of elastic fibers. Excess dye was removed by rinsing the slides in distilled water.

The tissue sections were then counterstained with Van Gieson's solution (Carl Roth GmbH, Karlsruhe, Germany), which contains picric acid and acid fuchsin, for 3–5 minutes. This step selectively stained collagen fibers red while background tissues appeared yellow. After the Van Gieson staining, the slides were washed briefly in distilled water to remove excess stain.

Differentiation was performed by dipping the slides in 96% ethanol until a clear distinction between the elastic fibers, collagen, and background tissue was visible under the microscope. Tissue sections were then dehydrated through ascending grades of ethanol, cleared in xylene, and coverslipped with a permanent mounting medium. This protocol resulted in elastic fibers appearing dark purple to black, collagen fibers stained red, and cytoplasmic structures yellow. Histological images were acquired with the digital slide scanner PANNORAMIC 1000 (3DHISTECH).

QUANTIFICATION AND STATISTICAL ANALYSES

Deep learning segmentation of whole slide H&E images

For learning a tissue segmentation model, we collected around ~5,000 representative pathologist annotations for 4 morphological sub-categories on H&E tissue morphology: "Carcinoma", "Stroma", "Necrosis", and "Normal lung" (e.g. including "Alveoli", "Capillaries", "Respiratory epithelium", "Vessels", etc.) for model training. For the segmentation model, we used a U-Net⁷⁶ architecture with a ResNet101 backbone.⁷⁷ We trained models over various hyperparameters for 50 epochs using the Adam optimizer⁷⁸ and selected the top five models based on the global F1 performance on a validation set. We then combined these five models into a mean ensemble, which achieved a global F1 performance of ~0.93 on a hold-out test set.

CosMx data processing

Registration, feature extraction, localization, decoding of the presence of individual transcripts, and deep learning-based cell segmentation (developed upon Cellpose⁷⁰) were performed as previously described.¹⁴ The final segmentation mapped each transcript in the registered images to the corresponding cell, as well as to subcellular compartments (nuclei, cytoplasm, membrane), where the transcript is located.

Unbiased transcriptomic clustering of segmented cells

For downstream analyses we used the package Seurat⁷¹ (v4.0.4) in R (v4.1, <https://www.R-project.org/>). For each section, we imported 3 matrices containing the gene expression, metadata and positions of segmented cells. We removed the negative probes from the gene expression matrix, defined a unique cell name and created a merged Seurat object with data from all the sections.

To identify cell types present in the TME, we adopted a very conservative filtering strategy removing only cells with less than 10 detected genes and removing genes detected in less than 1 cell. We then computed SCT-normalized and scaled gene expression counts⁷⁹ and computed the 50 most variable principal components (PCs). We selected the first 30 PCs to create a shared nearest neighbor graph and to compute a two-dimensional UMAP plot⁸⁰ used for data visualization in a low dimensional space. Finally, we partitioned the shared nearest neighbor graph using a resolution of 0.8 and identified 24 transcriptomic clusters.

Cell type annotation of transcriptomic clusters

To annotate cell types present in the TME, we identified marker genes enriched in each cluster for knowledge-based cell type annotation. Epithelial clusters, characterized by positivity to panCK immunofluorescent staining, comprised both tumor cells (*EPCAM*+ *S100A10*+) and non-malignant epithelial cells, including respiratory epithelium (*SCGB3A1*+), basal epithelial cells (*KRT5*+) and alveolar cells (*FGG*+). We also detected numerous stromal populations, including fibroblasts (*COL1A2*+) and vascular (*PECAM1*+) and lymphatic (*FABP5*+) endothelial cells, pericytes (*PDGFRB*+) and smooth muscle cells (*TAGLN*+) cells. We identified innate and adaptive immune cell populations, including macrophages (*CD68*+) and monocytes (*LYZ*+) cells, dendritic cells (*LAMP3*+) cells, mast cells (*KIT*+) cells, cytotoxic (*CD8A*+) and regulatory (*FOXP3*+) T cells, B cells (*IGHM*+) cells, plasma cells (*CD79A*+) and cycling immune cells (*MKI67*+) cells. Finally, we merged clusters with similar marker gene expression as probably related to different cellular states of the same cell type. Therefore, we annotated clusters '0' and '1' as fibroblasts, clusters '2' and '7' as macrophages and clusters '4', '5', '20', '22' and '23' as tumor cells.

Data integration with reference atlases

To compare gene expression profiles with published reference atlases, we performed label transfer using the standard Seurat pipeline. We integrated our data with the Human Lung Cell Atlas¹⁶ to annotate lung resident cell types and with a NSCLC single cell cohort¹⁷ to annotate tumor-specific cell types. For each reference dataset, we identified a subset of 900 shared ‘features’ (i.e. genes) using the `SelectIntegrationFeatures` function (`nfeatures = 900`) and pairs of ‘anchors’ (i.e. cells) between the reference and our query dataset using the `FindTransferAnchors` function (`normalization.method = "SCT"`, `reference.assay = "SCT"`, `query.assay = "SCT"`, `reduction = "pcaproject"`, `dims = 1:20`, `features = features`, `nn.method = "rann"`, `eps = 0.5`). Then, we leveraged the `TransferData` function (`anchorset = anchors`, `prediction.assay = TRUE`, `weight.reduction = "pcaproject"`, `dims = 1:20`, `eps = 0.5`) to score each cell in our query dataset for similarity with annotated cell types in the reference dataset.

3D alignment of spatial transcriptomic data

To align high-plex, single-cell resolved spatial transcriptomic data from 6 sequential, non-consecutive sections, we leveraged the Spatial Transcriptomics ImgLib2/Imaging Project (STIM).¹⁵ With STIM, we first converted our spatial transcriptomics data to the n5 image format for efficient storage and processing using the ‘st-resave’ function. In doing so, we assigned a channel to each gene and modeled gene expression values as pixel intensities at the center of the segmentation mask. Then, we applied the ‘st-align-pairs’ function to align each section to the one above and below ($r=1$) using the Scale Invariant Feature Transform (SIFT)⁸¹ according to the expression of the 15 genes with highest standard deviation ($n=15$). Finally, we applied the ‘st-align-global’ function to identify a global optimum that minimizes the distances between all corresponding points across all pairs of slices (`–absoluteThreshold 100 –sf 0.5 –lambda 0.5 –skipICP`).

Identification of 2D and 3D cellular neighborhoods

Cellular neighborhoods in 2D and 3D were computed with a custom Python script as follows. First, for a given cell, the Euclidean distances in 2 or 3D between that cell and all other cells in the dataset were computed. This set of distances was then filtered to remove distances greater than $r = 50 \mu\text{m}$, resulting in a list of neighboring cells for that given cell. This list was finally used to construct the 2D and 3D neighborhood matrices by counting the number of cells for each of the 18 cell types present in each cellular neighborhood. By design, 2D neighborhoods included a $50 \mu\text{m}$ -radius circular area ($\pi r^2 = 7853.98 \mu\text{m}^2$) in the section where the center cell is located, while their 3D counterparts also comprised two $40 \mu\text{m}$ -radius circular areas (each $\pi r^2 = 5026.55 \mu\text{m}^2$) in the sections immediately above and below in the z plane ($30 \mu\text{m}$ distance).

Unbiased identification and annotation of 2D and 3D multicellular niches

To identify 2D/3D multicellular niches in the TME, we imported the 2D/3D neighborhood matrix as a new assay in Seurat. We excluded cells with incomplete 3D neighborhoods, namely those located in sections 4 and 34 and those within $50 \mu\text{m}$ from the edges of sections 6, 12, 18 and 24. We then performed UMAP dimensionality reduction and clustering (`resolution = 0.3`). 3D neighborhoods analysis returned 13 clusters (Figure S1A). Furthermore, we merged clusters ‘3’, ‘10’ and ‘12’ as ‘T cell niches’ and clusters ‘5’ and ‘9’ as ‘airways’ given their shared neighborhood composition and spatial patterns (Figures S1B and S1C). In this way, we identified a total of 10 unique 3D niches, which we annotated based on the average cell type counts per 3D neighborhood: ‘tumor core’ (Tumor cells^{high}, Fibroblasts^{low}, Macrophages^{low}), ‘tumor surface’ (Tumor cells^{high}, Fibroblasts^{mid}, Macrophages^{mid}, Cytotoxic T cells^{low}), ‘airways’ (Respiratory epithelium^{high}, Basal epithelial cells^{high}), ‘alveoli’ (Alveolar cells^{high}), ‘desmoplastic stroma’ (Fibroblasts^{high}, Plasma cells^{low}), ‘vascular stroma’ (Fibroblasts^{mid}, Vascular endothelium^{mid}, Pericytes^{mid}), ‘smooth muscle’ (Smooth muscle cells^{high}), ‘Macrophage niche’ (Macrophages^{high}, Tumor cells^{mid}), ‘Dendritic cell niche’ (Dendritic cells^{high}, Tumor cells^{mid}, Macrophages^{mid}, Cytotoxic T cells^{mid}, Regulatory T cells^{low}) and ‘T cell niche’ (Cytotoxic T cells^{high}). At the same time, 2D neighborhoods analysis returned 15 clusters. Similarly, we merged clusters ‘8’, ‘10’ and ‘13’ as ‘tumor core’, clusters ‘2’ and ‘3’ as ‘tumor surface’, clusters ‘5’ and ‘12’ as ‘airways’ and clusters ‘4’ and ‘14’ as ‘T cell niches’ and identified 10 multicellular niches, which overlapped with 3D ones, with the exception of ‘dendritic cell niches’ identified only in 3D and ‘macrophage-rich stroma’ (Fibroblasts^{mid}, Macrophages^{mid}) identified only in 2D.

Ligand spatial activity scores in 2D and 3D cellular neighborhoods

To estimate the spatial activity of a specific ligand, we first downloaded manually-curated, literature-supported receptor ligand pairs from the CellChat Human database²⁰ and selected those in which both the receptor and the ligand were present in our 960-gene panel. For each center cell, we quantified the spatial activity of 164 ligands in its 2D and 3D cellular neighborhoods. To quantify the activity of each ligand in a given cellular neighborhood, we first evaluated single pairs of interacting cells comprising the center cell and one of its neighbors. For each pair, we computed the geometric mean of receptor expression in the center cell and ligand expression in the neighbor cell. In this way, we required the non-zero expression of both receptor and ligand to have positive pair scores. We then compute the overall ligand activity score for a specific cellular neighborhood summing all the pair scores having the center cell as receiver. In the case of ligands paired with multiple receptors, we summarized the ligand activity as the sum of the interactions with each of the associated receptors.

ECM composition analysis

To quantify ECM levels of collagen and elastin in section 4 cellular neighborhoods, we first imported cropped and aligned section 3 SHG TIFF images in R using the `grDevices` package (v. 4.1.3). We then normalized the collagen and elastin channels by dividing the pixel intensities by the maximum value in the respective channel. Finally, we quantified the mean collagen and elastin pixel intensities in the square with side $2 \times 50 \mu\text{m}$ centered on the segmentation center of each cell in section 4.

Unbiased identification of ECM compartments

To identify ECM compartments, we used k-means clustering of the scaled collagen and elastin intensities per cell as implemented in `kmeans` function of the R package `stats` v4.1.3. We selected $k=3$ based on the screeplot.

Fibroblast transcriptomic clustering and annotation

To identify transcriptomic states of the fibroblast in the TME, we selected cells annotated as fibroblasts with more than 100 detected transcripts for unsupervised clustering as described above, this time selecting the first 5 PCs and identifying 6 clusters and a resolution = 0.15. We then identified marker genes enriched in each cluster for literature-based cluster annotation^{82–86}: ‘matrix fibroblasts’ (*LUM+* *MGP+* *TIMP1+*), ‘myofibroblasts’ (*FN1+* *COL11A1+* *ACTA2+*), ‘activated fibroblasts’ (*JUN+* *FOS+* *IGF1+*), ‘antigen-presenting’ (*CD74+* *HLA-DRB1+*), ‘*CCL19+* reticular’ and ‘*CXCL10+* reticular’ fibroblasts.

Tumor pseudotime analysis

To reconstruct their molecular dynamics, we ordered tumor cells according to their pseudotime. We first generated a Seurat object including only tumor cells using the `subset` function and then re-normalized gene expression counts using `SCTransform`. We then selected the top 400 variable genes and grouped them in 5 PCs using the `RunPCA` function for downstream analyses. These included UMAP embedding using the `RunUMAP` function and pseudotime analysis. For the latter, we converted the Seurat object into `SingleCellExperiment` format using the R package `SingleCellExperiment` (v1.16.0⁷² and then used the `slingshot` function of the R package `slingshot` (v2.2.1)⁸⁷ to compute tumor cell pseudotime. Finally, we converted pseudotime scores to ranks (between 0 and 1) and added them as metadata in the Seurat object for plotting.

Preprocessing of imaging data

To stitch and register the .czi image files, acquired on the Zeiss AxioScan7 widefield microscope, the ASHLAR algorithm (v 1.17.0)⁸⁸ was used. To correct the tissue autofluorescent background signal, we performed background subtraction. Images were acquired before the first round of antibody staining; using the same settings for each channel (only exposure time was modified). The software package from github.com/SchapiroLabor/Background_subtraction was used (v 0.3.3) based on the following formula:

$$Marker_{corrected} = Marker_{raw} - \frac{Background * Marker_{exposure\ time}}{Background_{exposure\ time}}$$

Registration of IF and CosMx images

The IF multi-channel image stack from Section 12 was registered to the CosMx images of Section 10. To do this, the IF data stored as pyramidal OME-TIFF images were cropped into a rectangular region of interest (ROI) using `bftools` from `Bio-Formats` (v6.11.1).⁸⁹ This was done to exclude parts of the tissue outside CosMx ROI, reducing the overall size of the images and simplifying the registration process. The 24 contiguous fields of view of CosMx raw imaging data for Section 10 were then stitched into a single image using the `Grid/Collection stitching v1.2` plugin in `Fiji` v1.53t.⁷⁴ The average z-stack projection of the stitched stack was exported as a pyramidal OME-TIFF image. Rigid and affine registration was performed using `wsireg` 0.3.7 with default parameters, with the full IF stack of Section 12 as the moving image, and the stitched CosMx stack of Section 10 as the fixed (target) image.

Niche enrichments

To identify the preferential localization of a group of cells g in a specific niche n , we compared the observed and expected counts of g cells in niche n . The expected counts are computed under the assumption of random, independent distribution of cells belonging to group g and niche n . To compute expected counts, we simply multiplied the total abundance of g cells in the TME and the fraction of niche n in the TME. We then compute the \log_2 fold changes as the \log_2 of the ratio between observed and expected counts. In this way, we quantified the enrichment of infiltrating tumor cells, fibroblast states and cell types across all 3D niches and ECM compartments.

Quantification and visualization of 3D cellular density

We quantified the 3D spatial density of a group of cells g and visualized its 2D projection using the `geom_density_2d_filled` function from the `ggplot2` package (v 3.5.0) using $\alpha=0.5$ and $h=5.6 \times 700$. In this way, we quantified and visualized the 3D density of cytotoxic T cells, mesenchymal-like tumor cells (defined as pseudotime rank > 0.75), and myofibroblasts.

3D rendering of tissue niches, gene expression and ligand activity scores

Three-dimensional visualizations were generated by downscaling and mapping the spatial coordinates of segmented cell centroids onto 300x300 images along the xy-axes, using data from sections 10, 16, 22 and 28 along the z-axis. From these, 300x300x100 voxel data was constructed by interpolating 25 intermediate sections between each of the four sections using weighted Convolutional Wasserstein barycenters [93]. Voxel data were exported as TIFF files and visualized using ParaView v5.10⁷³ as surface or volumetric representations.

Statistical methods

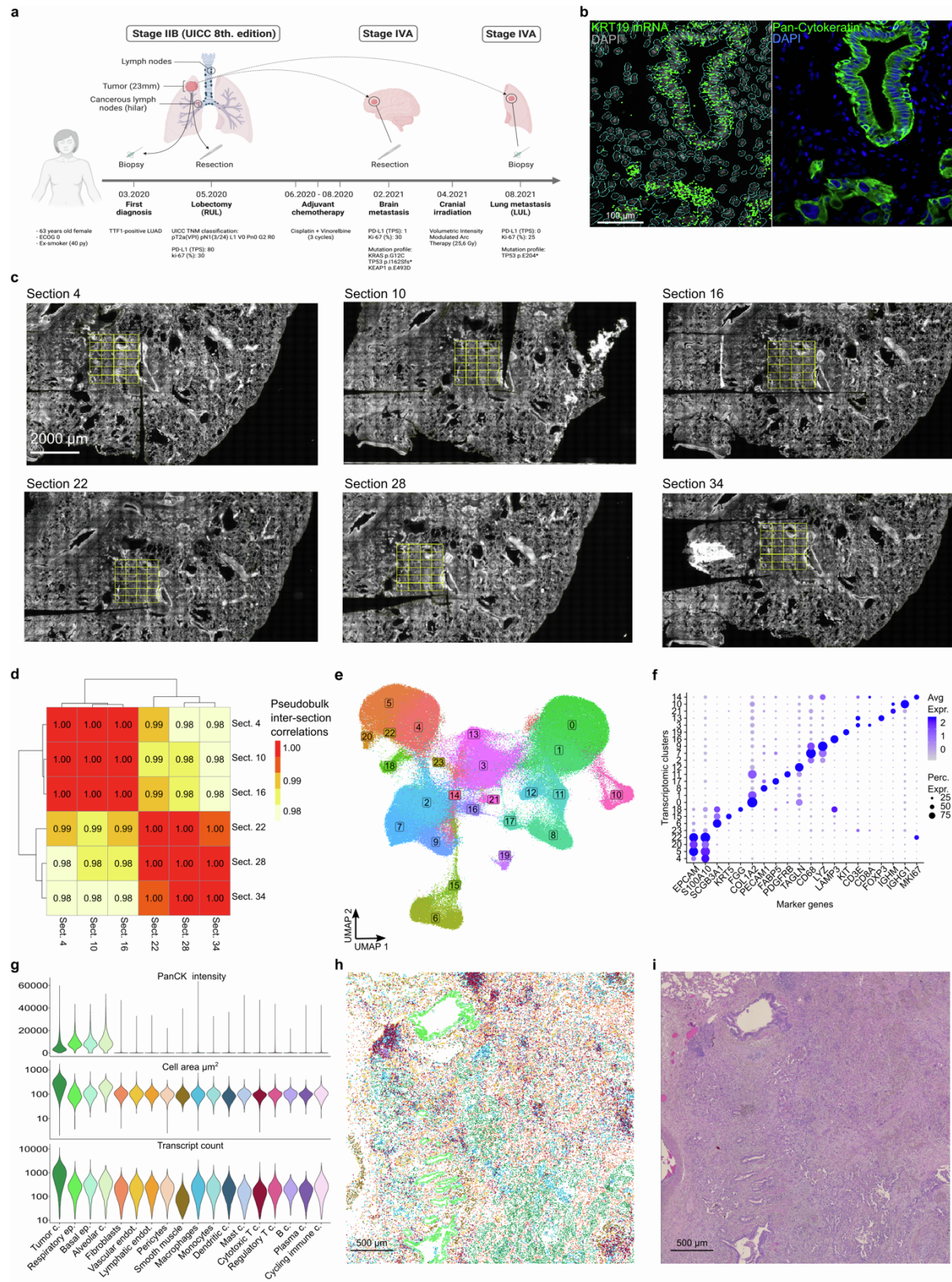
Cluster-specific marker genes used for cell type and fibroblast state annotation, niche-specific differentially expressed genes in a specific cell type (including tumor cells, fibroblasts and macrophages) were identified using a Wilcoxon Rank Sum Test comparing the expression of all genes in the group of interest versus all the remaining cells as implemented in the FindAllMarkers function in the Seurat R package (v. 4.0.4). To identify differential genes and receptor-ligand interactions, we first computed the average SCT-normalized expression or spatial activity score across all cells inside a group and then computed the \log_2 fold change against the mean of all cells outside the group. We also computed the percentage of expressing/receiving cells inside and outside the group of interest. Only genes/ligands surpassing both a \log_2 fold change and percentage difference thresholds are considered differentially expressed/active. p-values added to violin and boxplots were computed through an unpaired t-test using the `stat_compare_means` function of the ggpubr R package (v 0.6.0). Computed p-values were adjusted using Bonferroni correction for multiple testing.

Supplemental information

Combining spatial transcriptomics and ECM imaging in 3D for mapping cellular interactions in the tumor microenvironment

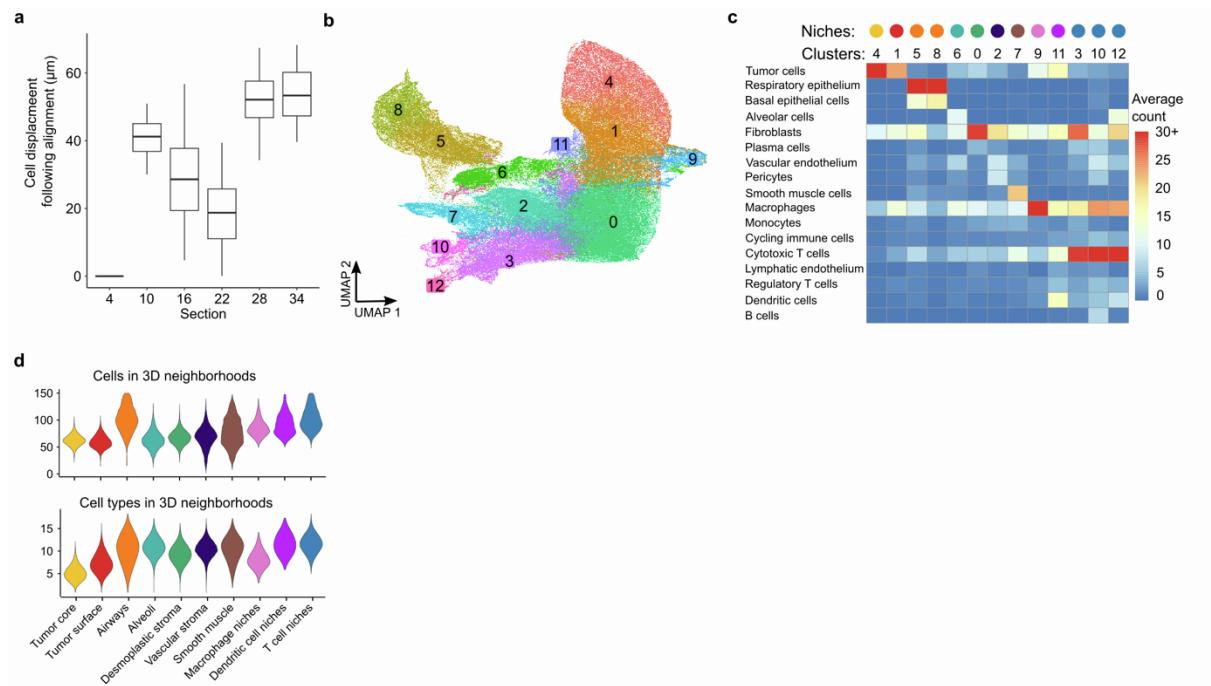
Tancredi Massimo Pentimalli, Simon Schallenberg, Daniel León-Periñán, Ivano Legnini, Ilan Theurillat, Gwendolin Thomas, Anastasiya Boltengagen, Sonja Fritzsche, Jose Nimo, Lukas Ruff, Gabriel Dernbach, Philipp Jurmeister, Sarah Murphy, Mark T. Gregory, Yan Liang, Michelangelo Cordenonsi, Stefano Piccolo, Fabian Coscia, Andrew Woehler, Nikos Karaiskos, Frederick Klauschen, and Nikolaus Rajewsky

SUPPLEMENTARY FIGURES

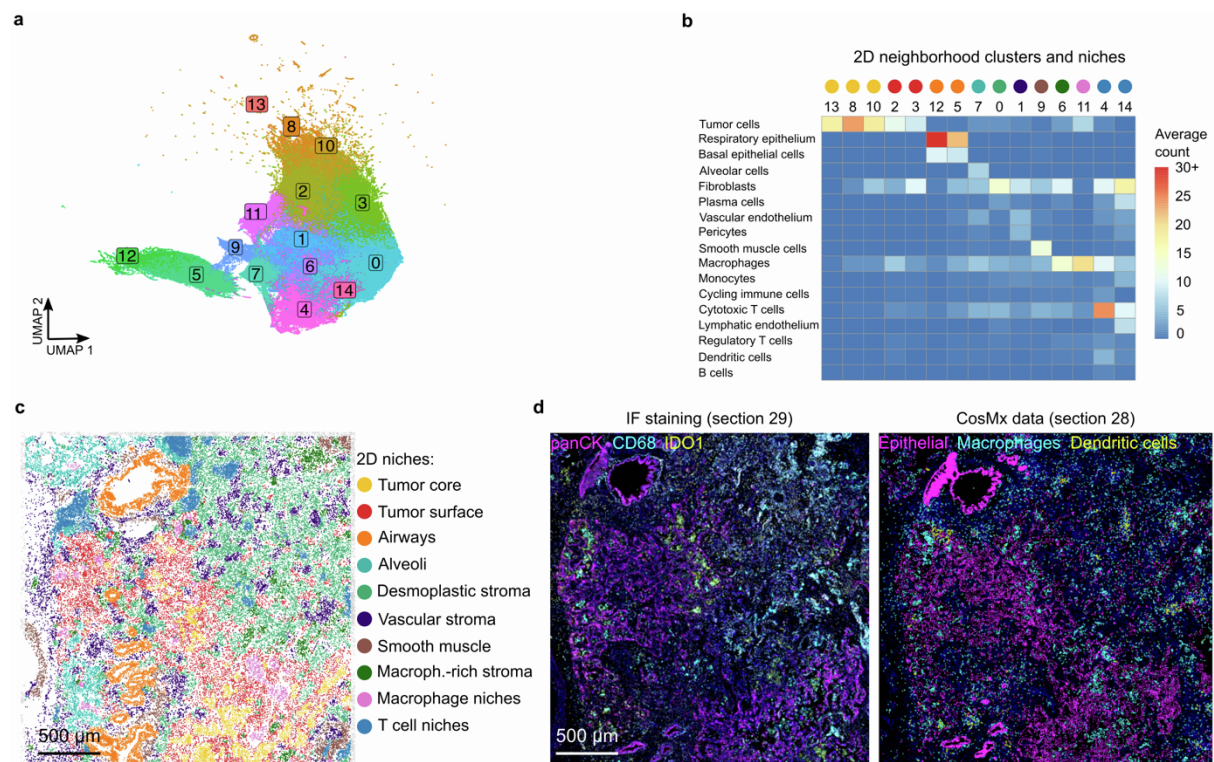


Supplementary figure 1, related to Figure 1. a) Schematics of characteristics, staging and

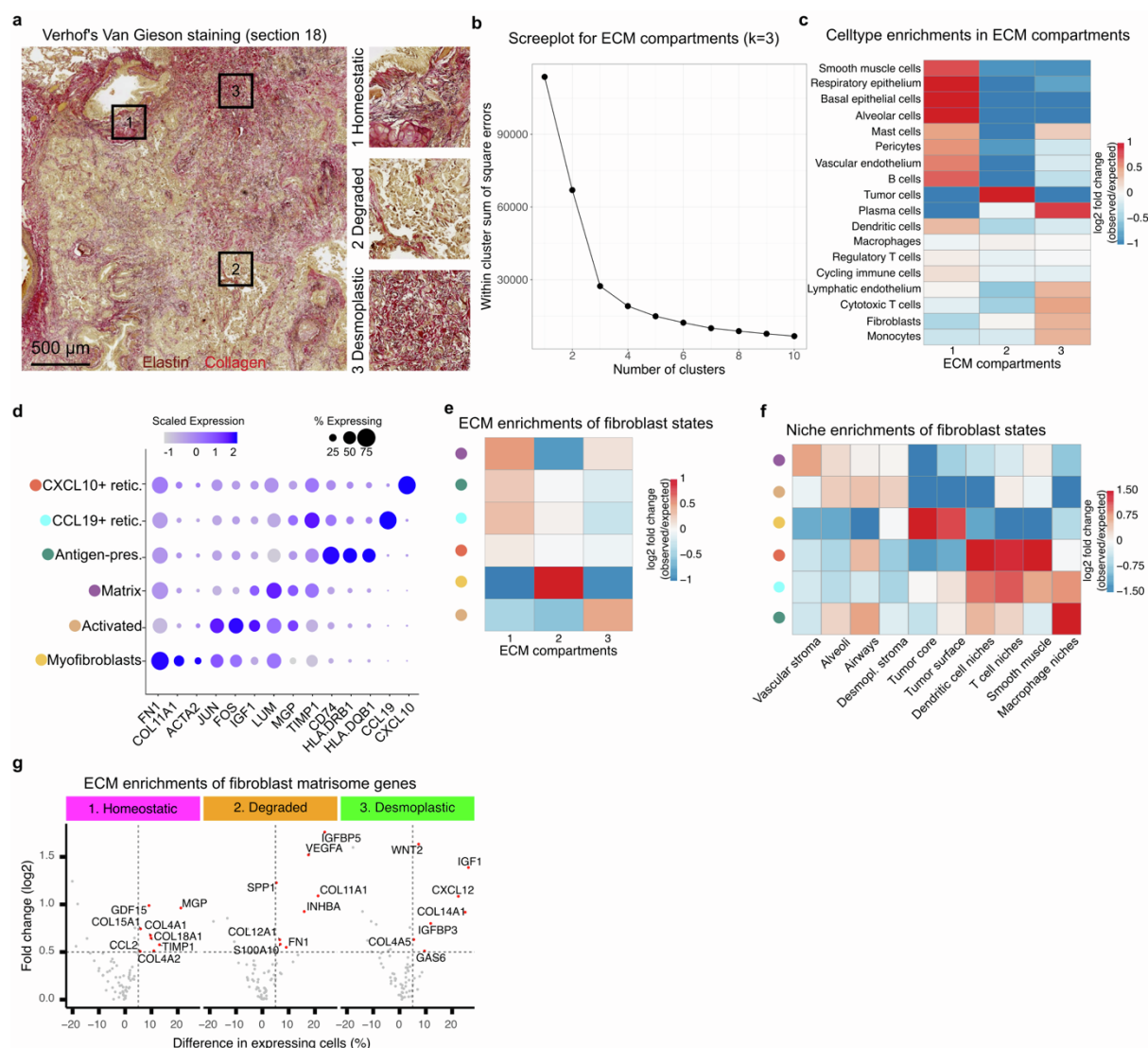
clinical history of the NSCLC patient under study. We investigated the lobectomy sample. **b)** Keratin 19 (KRT19) mRNA localization matches pan-cytokeratin immunostaining. Left: *KRT19* mRNA captured by CosMx (green: *KRT19* transcripts, gray: DAPI (nuclei), blue: cell segmentation masks). Right: pan-cytokeratin IF (epithelial cells, green; DAPI: blue). **c)** Whole slide images of the sections profiled with CosMx. Yellow: 24 fields of view in each ROI. **d)** Near-perfect correlation of gene expression across sections. Section-to-section Pearson correlation of aggregate gene expression profiles. **e)** UMAP of transcriptomic clusters. **f)** Cluster expression of canonical markers used for cell type annotations. **g)** Cell type distributions of pancytokeratin (panCK) immunofluorescence signal (top), segmentation mask area (middle) and transcript counts (bottom) per cell. **h)** Spatial plot of cell types in section 4. **i)** Tissue morphology by conventional hematoxylin and eosin staining in section 3.



Supplementary figure 2, related to **Figure 2**. **a)** Impact of 3D alignment on cellular positions. Boxplot of cellular shifts of cells in each section following 3D alignment. Section 4 was used as the anchoring section. **b)** UMAP of 3D cellular neighborhoods clusters. **c)** Cell type composition of neighborhood clusters. Heatmap showing the average 3D neighborhood count of each cell type across neighborhood clusters. Heatmap legend is clipped to 30 for visualization purposes. Clusters with similar composition are merged in a single multicellular niche: Clusters 5 and 8 as ‘Airways’, cluster 3, 10 and 12 as ‘T cell niches’. Niche color legend in Fig 2c. **d)** Violin plots of the number of neighbors (top) and different cell types (bottom) per 3D neighborhood across 3D niches.

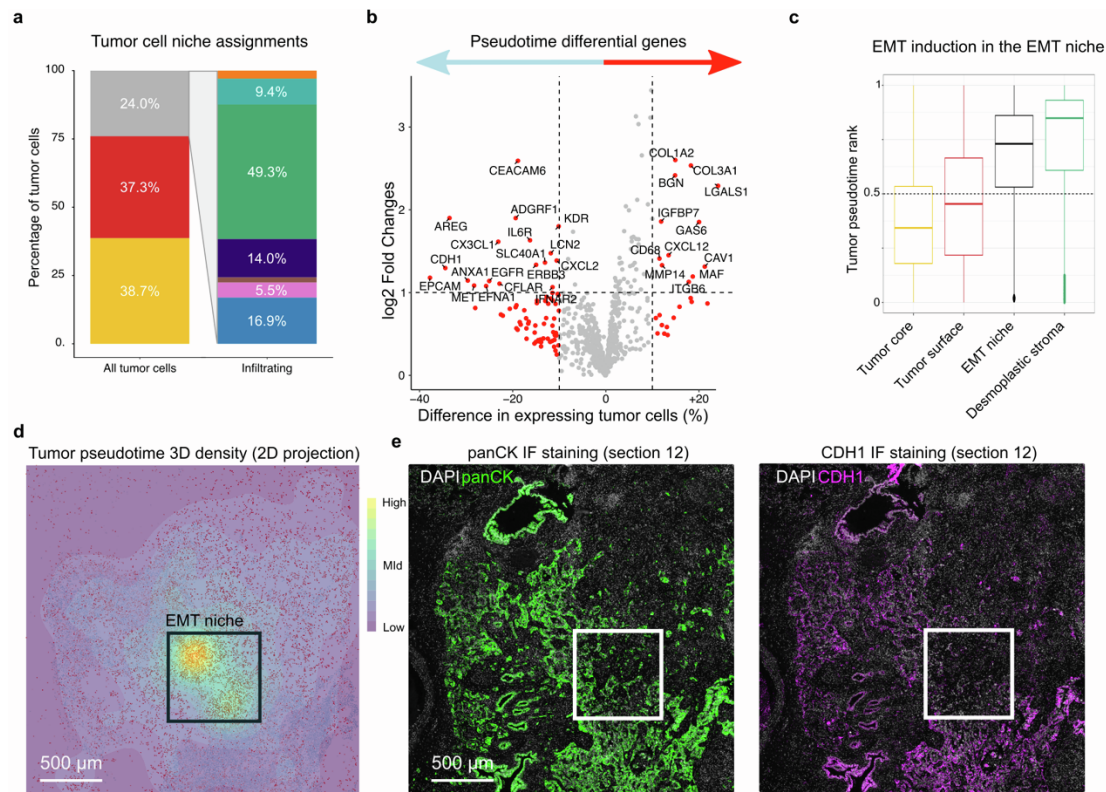


Supplementary figure 3, related to **Figure 3**. **a**) UMAP of 2D cellular neighborhoods clusters. **b**) Cell type composition of neighborhood clusters. Heatmap showing the average 2D neighborhood count of each cell type across neighborhood clusters. Heatmap legend is clipped to 30 for visualization purposes. Clusters with similar composition are merged in a single multicellular niche: Clusters 8, 10 and 13 as ‘Tumor core’, clusters 2 and 3 as ‘Tumor surface’, clusters 5 and 12 as ‘Airways’ and clusters 4 and 14 as ‘T cell niches’. **c**) Spatial map of 2D multicellular niches (section 10), gray: cells within 50 μ m of the section edge. **d**) Immunofluorescence validation of dendritic and macrophage niches. Left: Immunostaining (section 29) for nuclei (DAPI: blue) and tumor and normal epithelial cells (panCK: magenta), macrophages (CD68: cyan) and dendritic cells (ID01: yellow). Right: Spatial plot of celltypes (tumor and normal epithelial cells: magenta, macrophages: cyan, dendritic cells: yellow, others: blue) identified by CosMx in the adjacent section (section 28).

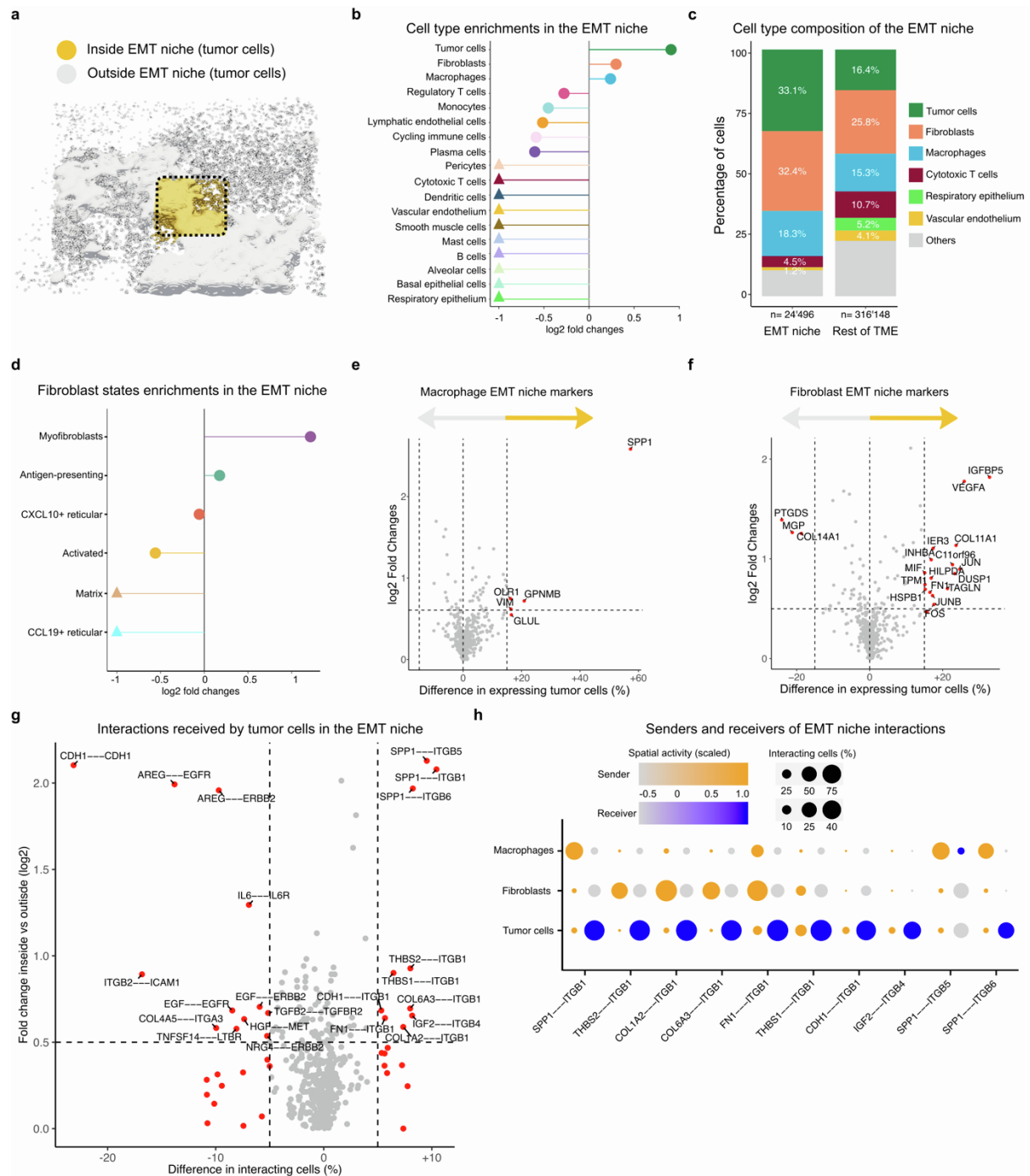


Supplementary figure 5, related to **Figure 5**. **a**) Verhoef's Van Gieson stain (section 18) validation of SHG imaging. Elastin (dark brown) and loose collagen fibers (red) characterize the homeostatic stroma (1), while the absence of elastin and thicker collagen bundles are found in the degraded (2) and desmoplastic (3) stroma, respectively. **b**) Heuristic identification of the optimal number of clusters for ECM compartments. Screeplot of k-means clustering of cellular neighborhood ECM composition. **c**) Cell types in the tumor microenvironment live in specific ECM compartments. Heatmap showing enrichment of cell types in ECM compartments. \log_2 fold changes are computed from the ratio between the observed and randomly expected number of cells per cell type in each 3D niche. **d**) Marker gene expression guides the annotation of fibroblast transcriptomic clusters. Dotplot of selected marker genes per fibroblast transcriptomic cluster. Dot size: percentage of cells expressing the gene. Dot color: scaled average expression. **e-f**) Fibroblast phenotypes are spatially linked with specific ECM compartments and multicellular niches. Heatmaps

showing enrichment of fibroblast phenotypes in ECM compartments (e) and multicellular niches (f). log₂ fold changes are computed from the ratio between the observed and randomly expected number of cells per fibroblast phenotype. **g)** The integrative analysis of ECM composition and fibroblast gene expression identifies matrisome genes enriched in ECM compartments. Scatter plot of matrisome gene expression in each niche. X axis: difference in the percentage of fibroblasts expressing a specific matrisome gene inside vs outside each ECM compartment. Y axis: log₂ fold changes of the average SCT-normalized fibroblast gene expression inside vs outside each ECM compartment. Labelled: enriched matrisome genes.



Supplementary figure 6, related to **Figure 6**. **a**) 3D neighborhoods enable the study of infiltrating tumor cells. Tumor cells assignment to multicellular niches identifies infiltrating tumor cells. Stacked barplots of all tumor cells (left) and infiltrating tumor cells (right) assignments to multicellular niches (yellow: tumor core, red: tumor surface, gray: outside the tumor bed, further color legend in Fig2c). **b**) Epithelial-to-mesenchymal transition (EMT) genes drive tumor pseudotime. Scatter plot of differential gene expression in tumor cells with late (rank > 0.5, right) vs early (rank ≤ 0.5, left) pseudotime. X axis: difference in the percentage of expressing tumor cells with late vs early pseudotime. Y axis: log₂ fold changes of the average SCT-normalized tumor gene expression. Red: genes with more > 5% expression difference labelled: pseudotime enriched genes. **c**) Tumor EMT is induced in the EMT niche and desmoplastic stroma. Boxplot of pseudotime rank in tumor cell neighborhoods across the EMT niche and the rest of the tumor bed and desmoplastic stroma. **d**) Mesenchymal tumor cells density peaks in the EMT niche (black box). 3D spatial density of tumor cells with late pseudotime (rank > 0.75). **e**) Immunofluorescence validation of CDH1 downregulation in the EMT niche (section 12). Left: Immunostaining for nuclei (DAPI: white) and tumor and normal epithelial cells (panCK: green). Right: Immunostaining for nuclei (DAPI: white) and epithelial phenotype (CDH1: magenta), white square: EMT niche.



Supplementary figure 7, related to **Figure 7**. **a**) The EMT niche is located at the interface between tumor surface and the surrounding stroma. 3D rendering of EMT niche (yellow), the tumor bed and infiltrating tumor cells (gray). **b**) Tumor cells, fibroblasts and macrophages are the only cell types enriched in the EMT niche. log2 fold changes are computed from the ratio between the observed and expected number of cells per cell type in the EMT niche. **c**) Evidence of EMT niche cellular remodeling. Stacked barplot of cell type assignment in the EMT niche (left) and the rest of the tumor microenvironment (right). Gray: cell types with <4% abundance in both regions. **d**) Myofibroblasts are enriched in the EMT niche. log2 fold

changes are computed from the ratio between the observed and expected number of cells per fibroblast phenotype in the EMT niche. **e)** SPP1, M2 and lipid-laden markers identify macrophages in the EMT niche. Scatter plot of differential gene expression in macrophages inside vs outside the EMT niche. X axis: difference in the percentage of expressing macrophages. Y axis: log2 fold changes of the average SCT-normalized macrophage gene expression. Labelled: EMT niche differential macrophage genes. **f)** VEGFA and IGFBP5 expression marks fibroblasts in the EMT niche. Scatter plot of differential gene expression in fibroblasts inside vs outside the EMT niche. X axis: difference in the percentage of expressing fibroblasts. Y axis: log2 fold changes of the average SCT-normalized fibroblasts gene expression. Labelled: EMT niche differential fibroblast genes. **g)** Integrin interactions dominate the signaling network in the EMT niche. X axis: difference in the percentage of tumor cells receiving a specific interaction inside vs outside the EMT niche. Y axis: log2 fold changes of the average interaction spatial activity inside vs outside the EMT niche. Labelled: differential interactions. **h)** Fibroblasts and macrophages stimulate tumor integrin signaling in the EMT niche. Dotplot of receptor-ligand interactions enriched in the EMT niche. Dot size: cell type-specific percentage of sender and recipient cells, dot color: cell type-specific scaled average interaction score as ligand sender (orange) and receptor receiver (blue).